ΠΑΝΕΠΙΣΤΗΜΙΟ ΠΑΤΡΩΝ
ΤΜΗΜΑ ΙΑΤΡΙΚΗΣ -ΤΜΗΜΑ ΦΥΣΙΚΗΣ
ΔΙΑΤΜΗΜΑΤΙΚΟ ΠΡΟΓΡΑΜΜΑ ΜΕΤΑΠΤΥΧΙΑΚΩΝ ΣΠΟΥΔΩΝ ΣΤΗΝ ΙΑΤΡΙΚΗ ΦΥΣΙΚΗ

ΜΕΛΕΤΗ ΨΕΥΔΟΕΙΚΟΝΩΝ ΜΕΤΑΛΛΙΚΩΝ ΟΡΘΟΠΑΙΔΙΚΩΝ ΕΜΦΥΤΕΥΜΑΤΩΝ ΣΤΗΝ ΤΟΜΟΓΡΑΦΙΑ ΠΥΡΗΝΙΚΟΥ ΜΑΓΝΗΤΙΚΟΥ ΣΥΝΤΟΝΙΣΜΟΥ

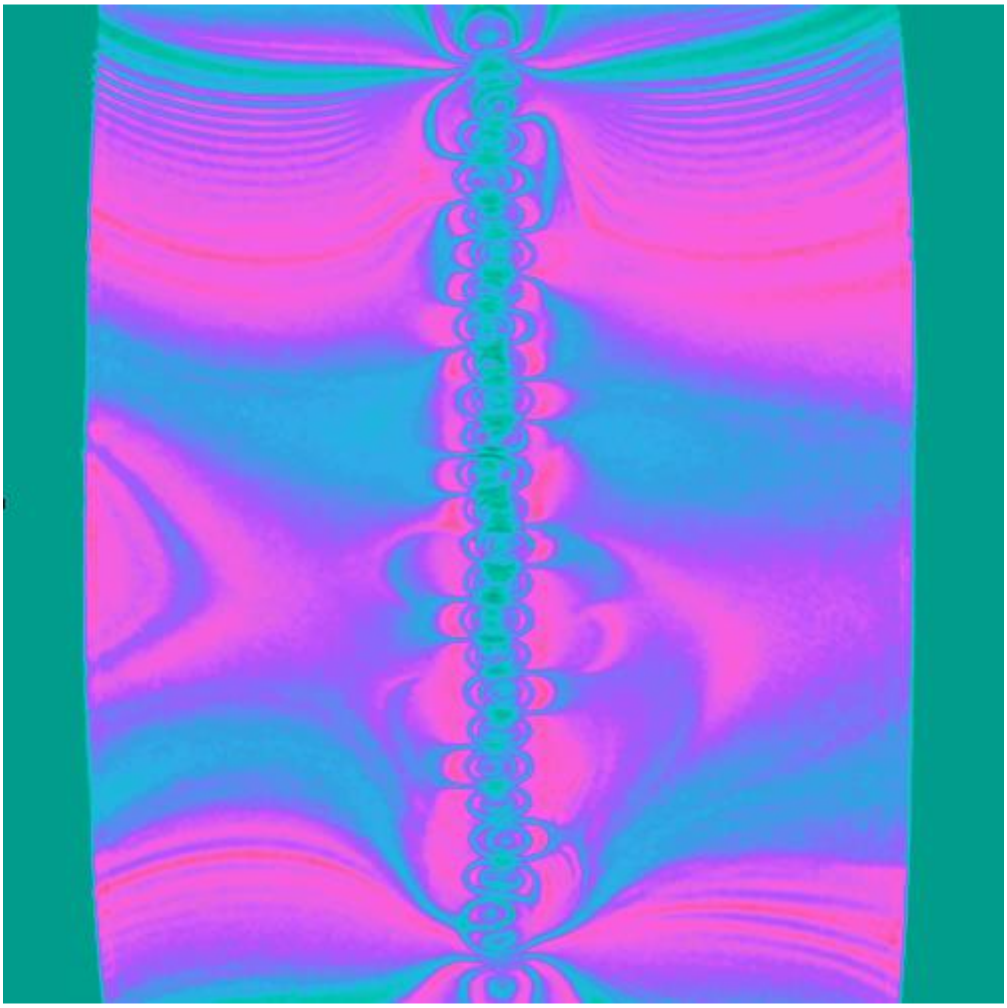

ΒΡΑΧΝΗΣ ΙΩΑΝΝΗΣ
ΔΙΠΛΩΜΑΤΙΚΗ ΜΕΤΑΠΤΥΧΙΑΚΗ ΕΡΓΑΣΙΑ
ΠΑΤΡΑ 2014

UNIVERSITY OF PATRAS
DEPARTMENT OF MEDICINE - DEPARTMENT OF PHYSICS
INTERDEPARTMENTAL COURSE OF POSTGRADUATE STUDIES IN MEDICAL PHYSICS

STUDY OF IMAGE ARTIFACTS OF METAL ORTHOPAEDIC IMPLANTS IN NUCLEAR MAGNETIC RESONANCE TOMOGRAPHY

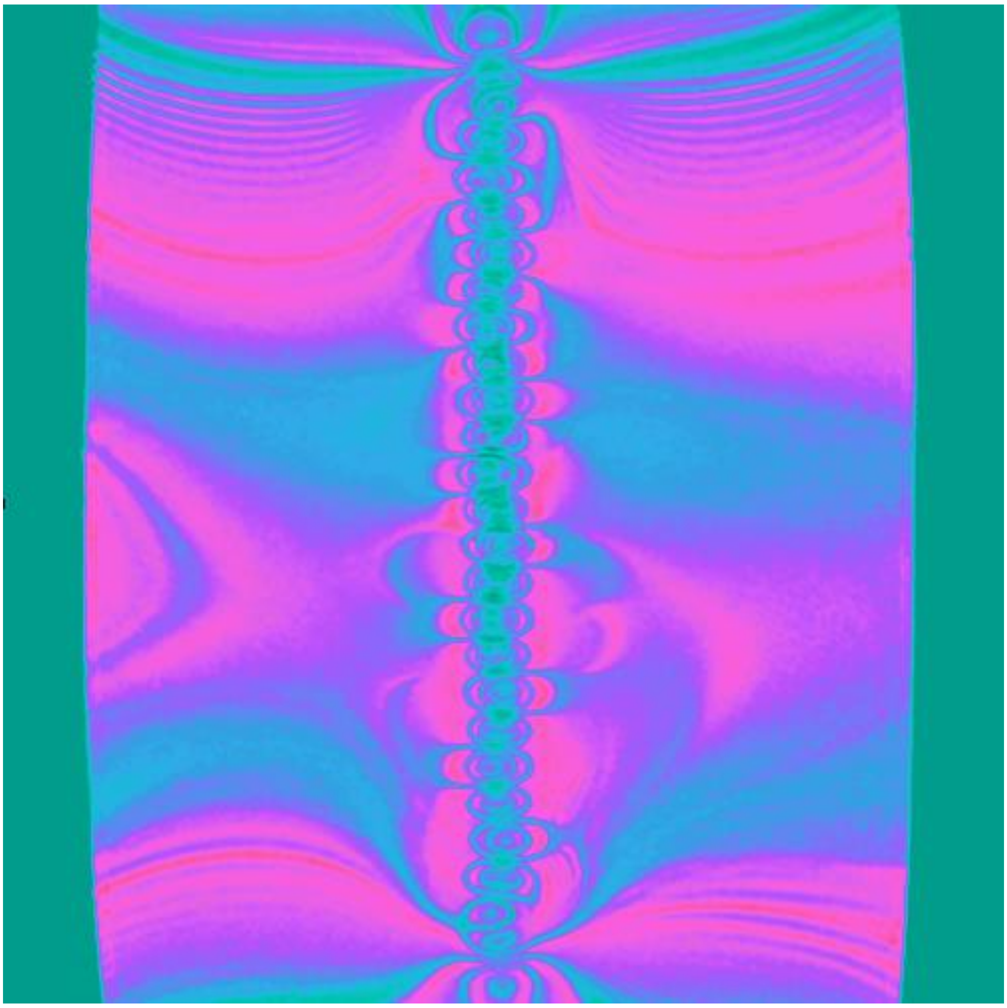

VRACHNIS IOANNIS,MD
MASTER THESIS
PATRAS 2014

SUPERVISOR

ASSOCIATE PROFESSOR L. COSTARIDOU
DEPARTMENT OF MEDICAL PHYSICS, MEDICAL SCHOOL, UNIVERSITY OF PATRAS

THREE MEMBER EXAMINATION COMITTEE

ASSOCIATE PROFESSOR L. COSTARIDOU
DEPARTMENT OF MEDICAL PHYSICS, MEDICAL SCHOOL, UNIVERSITY OF PATRAS

ASSOCIATE PROFESSOR TH. MARIS
DEPARTMENT OF MEDICAL PHYSICS, MEDICAL SCHOOL, UNIVERSITY OF CRETE

PROFESSOR EL. PANAGIOTOPOULOS
DEPARTMENT OF ORTHOPAEDICS, MEDICAL SCHOOL, UNIVERSITY OF PATRAS

ACKNOWLEDGMENTS

I wish to express my gratitude to my supervisor *Prof.L. Costaridou* who offered me the opportunity to deal with the interesting and evolving area of medical image processing. Her support and scientific guidance contributed the best to the completion of this research work.
I am grateful to *Prof. Th. Maris* for accepting the invitation to participate in my examination committee, for his assistance in the accomplishment of all the experimental measurements, his expert advice and his hospitality during my stay at Crete.
I am thankful to *Prof. El. Panagiotopoulos* for accepting the invitation to participate in my examination committee, for his scientific support and for the supply some of the implants used during the experimental procedure.
I am also thankful to *G Vlachopoulos*, for his valuable contribution to image processing and constructive recommendations during this work. Furthermore I would like to thank him for his trip to Crete in order to help me in the experimental procedure.
I express my warm thanks to *T. Jaber*, *K. Karaindros* and *F. Papadopoulos*, orthopaedic surgeons at the general Hospital of Amaliada, for the supply some of the orthopedic prostheses used in the experiments.
I would like to thank *T. Boursianis* and *S. Veneti*, for their help in the experiments at Crete and their hospitality and *S. Skiadopoulos* and *A. Karahaliou* for their assistance in the experiments that took place at Patras.
I would like to acknowledge the Director of the Postgraduate Course *Prof. G Nikiforidis* as well as all the professors of the Course, who gave me the opportunity to work in the fascinating area of Medical Physics

TABLE OF CONTENTS

THEORY

MATERIALS AND METHODS

LIST OF FIGURES

LIST OF TABLES

ΠΕΡΙΛΗΨΗ

Η εξέλιξη της ιατρικής και ειδικότερα της ορθοπαιδικής έχει κάνει ολοένα και περισσότερο συχνή την ύπαρξη ασθενών που φέρουν μεταλλικά εμφυτεύματα. Η απεικόνιση με μαγνητικό συντονισμό πλεονεκτεί σε σχέση με άλλες απεικονιστικές μεθόδους εξαιτίας της καλύτερης αντίθεσης που προσφέρει στους μαλακούς ιστούς και στην ευαισθησία στην ανάδειξη της φλεγμονής που συνοδεύει τις μολύνσεις και τις κακοήθειες. Η ύπαρξη μεταλλικών εμφυτευμάτων συνήθως υποβαθμίζει την ποιότητα της εικόνας και την καθιστά πολλές φορές μη διαγνωστική, ειδικά αν η περιοχή ενδιαφέροντος είναι κοντά στο μεταλλικό εμφύτευμα ή στην περίπτωση που αυτό είναι αρκετά μεγάλο. Μια σειρά από μεθόδους ή ακόμη και ειδικές ακολουθίες έχει προταθεί κατά καιρούς για να αντιμετωπιστεί η ύπαρξη των τεχνημάτων επιδεκτικότητας, όπως ονομάζονται τα artifact που έχουν σαν αιτία τους τις τοπικές στρεβλώσεις στο μαγνητικό πεδίο εξαιτίας μεταλλικών προθέσεων. Οι πιο αποτελεσματικές από αυτές παραμένουν μη διαθέσιμες για το ευρύ κοινό. Η ανάγκη για βελτιστοποίηση των συνθηκών απεικόνισης κάνει επιτακτική την ανάγκη για ποσοτικοποίηση του artifact στις διαφορετικές συνθήκες λήψεις.

Οι τεχνικές ποσοτικοποίησης του artifact που έχουν προταθεί μέχρι σήμερα βασίζονται στην ποιοτική ακτινολογική εκτίμηση (οπτική παρατήρηση) είτε σε μεθόδους τμηματοποίησης της περιοχής εικόνας του artifact που συνήθως στηρίζονται στην επιλογή αυθαίρετων τιμών κατωφλίου τόνων του γκρι. Μια πιο αντικειμενική και ακριβής μέθοδος αφορά στην αφαίρεση εικόνων γεωμετρικού αναλόγου (αντικείμενο ελέγχου- ομοίωμα) του εμφυτεύματος από την εικόνα που απεικονίζει το ίδιο το εμφύτευμα. Το ανάλογο είναι κατασκευασμένο από υλικό με παρόμοια μαγνητική επιδεκτικότητα προς το περιβάλλον του εμφυτεύματος. Η απεικόνιση ενός τέτοιου ομοιώματος, λαμβανομένης υπόψη και της συνεισφοράς του θορύβου, παρουσιάζει μηδενικό artifact επιδεκτικότητας σε σχέση με το πραγματικό εμφύτευμα. Το artifact στην περίπτωση αυτή ποσοτικοποιείται ως διαφορά ενέργειας εικόνας στην περιοχή του περιβάλλοντος υλικού ***[Kolind S et al,2004]***. Η τελευταία αυτή μέθοδος ενώ ποσοτικοποιεί με ακρίβεια το artifact δεν παρέχει πληροφορίες για τη θέση του στο χώρο.

Στην παρούσα μεταπτυχιακή εργασία, προτείνεται μία νέα, με βάση τα όσα γνωρίζουμε, μέθοδος ποσοτικοποίησης του artifact. Η μέθοδος αυτή βασίζεται στη γενεσιουργό αιτία του artifact, που είναι οι στρεβλώσεις του μαγνητικού πεδίου από την παρουσία του μεταλλικού αντικειμένου. Οι στρεβλώσεις αυτές εκφράζονται ως βαθμιδώσεις του μαγνητικού πεδίου. Οι βαθμιδώσεις του Μ.Π προκαλούν αντίστοιχες βαθμιδώσεις στην ένταση των τόνων του γκρι στην εικόνα. Αυτές οι βαθμιδώσεις μπορούν να αναδειχθούν αν εφαρμόσουμε κατάλληλο φίλτρο στην εικόνα που ανιχνεύει το μέγεθος/ πλάτος της βαθμίδωσης. Με αυτό τον τρόπο θα ανιχνευτούν τόσο περιοχές με υψηλό όσο και περιοχές με χαμηλό σήμα, απλοποιώντας έτσι τη διαδικασία, αφού δε χρειάζεται να ανιχνευτούν με ξεχωριστό αλγόριθμο περιοχές του artifact με πολύ διαφορετικές τιμές τόνων του γκρι. Στη συνέχεια η εικόνα που προκύπτει κατωφλιώνεται με αυτόματη μέθοδο που έχει προταθεί ***[Li & Lee 1993]*** και είναι διαθέσιμη στο περιβάλλον ανάλυσης εικόνας Image J.

Στο πρώτο τμήμα της παρούσας εργασίας αναπτύσσονται, συνοπτικά βασικές αρχές του πυρηνικού μαγνητικού συντονισμού και του τρόπου με τον οποίο δημιουργείται η δισδιάστατη εικόνα στο MRI. Ακολουθεί επίσης μια σύντομη περιγραφή του τρόπου με τον οποίο συμπεριφέρονται τα πιο κοινά υλικά όταν βρεθούν εντός του μαγνητικού πεδίου.

Όλα αυτά είναι αναγκαία για γίνει κατανοητός ο τρόπος που δημιουργείται το artifact μαγνητικής επιδεκτικότητας στην εικόνα που λαμβάνουμε. Στη συνέχεια αναπτύσσεται με λεπτομέρεια ο μηχανισμός και η φυσική που εμπλέκεται στη δημιουργία των artifact μαγνητικής επιδεκτικότητας.

Στο πειραματικό μέρος, εφαρμόζεται ο προτεινόμενος αλγόριθμος σε απεικονίσεις δύο εμφυτευμάτων (τιτανίου και αντιμαγνητικού χάλυβα) στις πιο κοινά χρησιμοποιούμενες ακολουθίες του μυοσκελετικού. Ο προτεινόμενος αλγόριθμος ελέγχεται ως προς την ικανότητα του να ποσοτικοποιεί το artifact με μία παραλλαγή της μεθόδου διαφοράς ενεργειών εικόνων ***[Kolind Sh,2004].*** Η μέθοδος αυτή ποσοτικοποιεί το artifact ως διαφορά ενέργειας της εικόνας του πραγματικού εμφυτεύματος από εικόνα γεωμετρικού αναλόγου με μηδενικό artifact (εικόνα αναφοράς). Στην περίπτωση μας χρησιμοποιήσαμε ως εικόνα αναφοράς την εικόνα με το ελάχιστο artifact (η οποία βάσει θεωρίας αντιστοιχεί στη λήψη με το υψηλότερο bandwindth). Επίσης θεωρήσαμε τη διαφορά θορύβου των διαφορετικών λήψεων αμελητέα ως προς τις τιμές έντασης (τόνοι του γκρι) του artifact, ώστε να μπορούμε να αξιοποιήσουμε το πεδίο των τιμών των τόνων του γκρι και όχι αυτό της ενέργειας της εικόνας. Η στατιστική επεξεργασία αναδεικνύει μέτρια ως ισχυρή θετική συσχέτιση των 2 αλγορίθμων. Πιθανοί λόγοι που δεν έχουμε σε όλες τις μετρήσεις ισχυρή ή πολύ ισχυρή συσχέτιση αποδίδονται πρωτίστως στην περιοχή της εικόνας που ποσοτικοποιεί η προτεινόμενη μέθοδος. Τμηματοποιώντας τις βαθμιδώσεις της εικόνας εστιάζουμε σε περιοχές που υπάρχει έντονη μεταβολή των τιμών του γκρι. Παρόλα αυτά το artifact μπορεί κατά περιπτώσεις να περιλαμβάνει και ομοιογενείς περιοχές εικόνας με παραπλήσιες τιμές του γκρι. Αυτές είναι περιοχές που δεν τμηματοποιεί (ανιχνεύει) η προτεινόμενη προσέγγιση. Μια ακόμη αιτία θα μπορούσε να είναι η μη αξιολογήση της συνεισφοράς του θορύβου στις διαφορετικές λήψεις (bandwidths).

Η απώλεια τέτοιων περιοχών δεν μειώνει την αξία του αλγορίθμου, αφού αποτελεί μια αντικειμενική μέθοδο, ανεξάρτητη από τον παρατηρητή, επαναλήψιμη και ικανή να οριοθετήσει το artifact στο χώρο. Δεν της επιτρέπει παρόλα αυτά να χρησιμοποιηθεί σαν μέθοδος απόλυτης ποσοτικοποίησης του artifact. Μπορεί να χρησιμοποιηθεί για την πραγματοποίηση συγκρίσεων ιδανικά σε συνθήκες λήψεις που αφορούν την ίδια ακολουθία. Ο συνδυασμός της με ένα επιπλέον αλγοριθμικό βήμα, όπως ένα βήμα που θα ανιχνεύονται χαρακτηριστικά της εικόνας σε συνδυασμό με την οριοθέτηση του artifact που έχει προηγηθεί, μπορεί να δώσει ένα ισχυρό εργαλείο τμηματοποίησης της εικόνας με εφαρμογές που θα μπορούν να επεκταθούν από τη χρήση σε ομοιωμάτων ως εργαλείων για την ποσοτικοποίηση του artifact και στην καθημερινή κλινική πρακτική.

ABSTRACT

The number of patients who have undergone some kind of internal fixation or joint replacement is increasing thanks to the development of technology and orthopaedics. All these patients carry metal implants. Magnetic resonance imaging has an advantage over other imaging methods, due to its superior soft tissue contrast and to its sensitivity in detecting the inflammation which is present at infections and malignancies. However metal implants usually deteriorate the image quality and as a result affect the accuracy of the diagnostic procedure. This is the case when the region of interest is in the proximal vicinity of the implant, or the implant is large enough. A number of MRI sequences have been proposed in order to overcome the artifact that comes from metal implants, more formally known as susceptibility artifact. However the most effective of them, are not widely available. The need for optimization of MR imaging at the presence of metal implants presupposes the development of methods capable of quantifying the artifact under various imaging sequences and conditions.

Most artifact quantification techniques proposed until now, are usually based on the visual observation (experienced radiologists) or at image segmentation methods. These segmentation methods, segment the image based on arbitrary selected gray values (thresholds). A more objective and precise quantification method relies on the subtraction of images of a zero artifact replica (test object) from those of the real metal implant. The copy is constructed from material with similar values of magnetic susceptibility with its environment (usually water). The images deriving from the copy if we take in consideration the noise differences, have no susceptibility artifact. In this method artifact is quantified as energy differences between the two images ***[Kolind S et al, 2004]***. Since the acquisition conditions are identical except the presence of susceptibility artifact in the image depicting the real metal object, the energy difference is used to quantify the artifact. While the method quantifies the artifact, giving precise values, it does not inform us for its position in space

At this thesis we proposed a new, to our knowledge, method of artifact quantification. It is based in the physical cause of the artifact, which are the gradients of the magnetic field, which derive from the presence of the metal implant. The gradients of the magnetic field create corresponding gradients at the gray scale values of the image. These gradients may be detected if we apply suitable filter which detects the amplitude of the gradient. In this way we detect both regions with signal void (low signal intensity) and signal pill ups (high signal intensity). That means that we do not have to apply two different operators to segment two regions of the artifact with so different signal intensity values. Then the image is thresholded using a fully automated algorithm, proposed by ***[Li & Lee 1993].*** This algorithm is available in image analysis environment ImageJ.

At the first part of this thesis there are presented the basic principles of nuclear magnetic imaging image formation. The interaction of the most common materials with the magnetic field is also presented. All these are considered necessary to explain the generation of magnetic susceptibility artifact at the image acquired. The theory beyond the magnetic susceptibility artifact generation is then explained in detail.

At the experimental part of this thesis, the proposed algorithm is applied to the imaging of two implants (made of titanium and antimagnetic stainless steel) at the sequences which are most commonly used to musculoskeletal MRI. The proposed algorithm is compared with a variation of the method of the image energy differences proposed by ***[Kolind Sh, 2004].*** This method quantifies the artifact as energy difference of image of the real implant from the image of a replica with zero susceptibility artifact (reference image). In the present thesis the image of lower susceptibility artifact (obtained at higher bandwidth) is considered as reference image. In our case it is assumed that the energy difference among different bandwidth acquisitions is negligible in relation to the susceptibility artifact amplitude. This assumption allows as to use instead of energy differences, the differences in the gray scale values of the image instead. Statistical analysis showed moderate to strong positive correlation between the two methods. Possible reasons of not obtaining strong correlation at all measurements is due to the regions of the image that the proposed algorithm quantifies. By segmenting regions of high gradient, we focus mainly at regions where there is high variation at the gray scale values. However, in many cases nearly homogeneous regions of an image, with little or no alteration in gray scale values, may also be considered as artifact. These areas are not segmented as artifact when the proposed algorithm is applied. More over the assumption of considering negligible the noise contribution between the different acquisitions may be an oversimplification.

Nevertheless, the proposed algorithm, is an objective repeatable and observer independent method. Moreover it is capable of determining the boundaries of the artifact in image space. It is not intended to be used as a method of absolute quantification of the susceptibility artifact. It should be used as means of comparison of acquisitions concerning the same sequence. Its combination with an additional algorithmic step, such as one which detects image features may result in a powerful tool of image artifact quantification. This more sophisticated version of this proposed algorithm should be adequate enough to quantify the artifact not only at phantom models but even at the everyday clinical practice.

INTRODUCTION

The evolution of orthopaedics involves more and more the use of metal orthopaedics implants. Metallic implants are commonly used in orthopaedic surgery to fixate fractures, replace arthritic joints and align and immobilize vertebra. Total hip arthroplasty (THA) is the most practiced orthopaedic surgery procedure in elderly , with more than 800.000 per year around the world ***[White LM et al,2000]***. In United States there were 325.000 spinal fusions performed in 2003 and 450.000 total knee arthroplasties performed in 2002 ***[Kurtz et al,2005]***
The current standard imaging technique for complications associated with ~~the complications~~ of these devices is the plain radiograph. However the plain radiograph depicts three dimensional structures in two dimensions and requires the x ray beam to be oriented exactly parallel to the bone - implant interface ***[Resnick D,2002].*** Computed tomography is a better alternative since it depicts the entire bone - implant interface in three dimensions. However this technique suffers from streak / beam hardening artifacts and data loss ***[Mi -Jung Lee et al, 2007].*** Moreover radiography and CT are not so sensitive in soft tissue abnormalities and bone marrow edema.

Magnetic resonance imaging (MRI) is the best imaging method for diagnosing patients with metal prostheses, due to its superior soft tissue contrast. However, the presence of metal implants creates artifacts that hinder the diagnosis. In the static magnetic field of the MR scanner, new magnetic gradients are generated due to the metallic implants. Although differences in susceptibility are present in human body (such as the tissue air or tissue bone interfaces), the differences are not so large as these between metal and tissue. Many techniques and pulse sequences have been proposed in order to reduce metal artifacts. The most simple of them propose adjustments which have to do with the orientation of the implants, the receiver bandwidth, echo train length, selection of spin echo sequences, or voxel size to name some ***[Mi -Jung Lee et al, 2007]***. More sophisticated techniques require dedicated systems, with special pulse sequences not commonly available. The most known of them are view angle tilting ***[Z. H. Cho et al, 1988],*** metal artifact reduction sequence (MARS), SEMAC ***[Wenmiao et al, 2009***] and MAVRIC ***[Koch et al, 2009]***

The number and the complexity of the methods proposed to reduce or ideally eliminate the susceptibility artifact indicate that there is no gold standard technique for metal artifact reduction. More over the best of them are considered exotic pulse sequences since they are not available in everyday practice. The above, make necessary procedures of optimization of the acquisition parameters. So there is obvious need for experimental processes for susceptibility artifact quantification.

In this thesis a novel method of susceptibility artifact quantification is proposed. The method is quantitative as compared to visual observations, representing the clinical de facto standard. The segmentation algorithm is based on the physics of artifact generation. By assuming that image gradients capture the distortions of the magnetic field we measure image magnitude gradient. Then thresholding is applied using an automatic cross entropy method. The method is fully algorithmic, observer independent and repeatable.

LITERATURE REVIEW -THESIS

Susceptibility artifacts due to metal implants are known since first days of NMR imaging. Many articles were published in early eighties. ***[Augustiny et al, 1987]*** give as a qualitative description of the basic characteristics of this kind of artifacts based on in vitro and in vivo studies. They described three features of susceptibility artifact. The geometric distortions are most marked in regions of shape change such as edges or pinpoints. There are regions of signal loss with either sharp margins or a gradual signal loss toward the implant and linear sharply demarcated areas of very strong signal. Theory predicts the existence of these areas of low and of high signal. This observation is important because we have to notice that the susceptibility artifact may be present anywhere in the gray scale.

Further description of the shape of the artifact is given in another article ***[Jin-Suck Suh et al, 1998].*** Susceptibility artifact has cloverleaf shape when a long axis of the screw is perpendicular to the main field direction, whereas when the long axis of the implant is parallel to the main magnetic field the artifact is round or oval in shape. It was also observed that the middle lobes of the cloverleaf were oriented along the frequency encoding direction. Alteration between frequency and phase encoding direction results in alteration of the direction of the middle lobe of the cloverleaf, in order to be oriented along the frequency encoding direction. In experiments it was found that metal artifacts from pseudo -cylindrical structures such as screws or stems may follow a certain pattern looking like a cloverleaf or an arrow ***[Vandevenne et al, 2007]***.

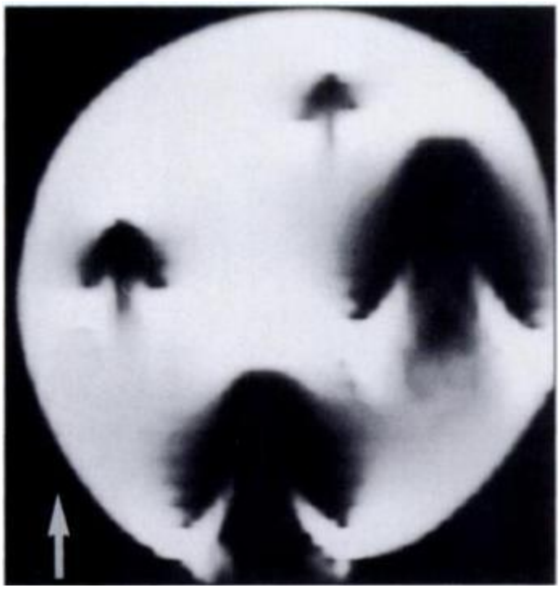

FIG.1: **Cloverleaf artifact derived from titanium and stainless steel screws. [Adapted from Jin-Suck Suh et al, 1998]**

Quantification of the susceptibility artifact is not an easy task. Its shape is irregular and largely unpredictable, while the borders of the artifact are not always clear. The most widely acceptable approaches of qualitative assessment were carried out by experienced radiologists. In such studies the number of observers plays a critical role. Rudish et al ***[Rudish et al,1998]*** quantified the artifact created from spinal fusion implants, both in vitro and in vivo, using three independent viewers. The dorsal part of the artifact was measured. In vitro (phantom) they used another estimator for the artifact. The real extend in millimeters from the front wall of the phantom to the most dorsal point where the MRI signal was superimposed to the artifact, was used. In another study by Hayter et al ***[Hayter et al, 2011]*** the observers had to rate the extend of the artifact in shoulder arthroplasties, according to the number of adjacent anatomical structures which were visible. The greatest score was given when synovium, bone- prostheses interface or supraspinatus tendon were visible. Even in more recent studies quantitative analysis is based as distance measurements ***[Sang-Young Zho et al , 2012****]* measured the in plane distortion as the distance from the object edge to signal pile up or void. Through plane distortion was measured as the number of slices that showed signal pile ups or voids. As early as in 1998, ***[Jin-Suck Suh et al, 1998]*** tried to quantify the artifact through two measurements. When the cloverleaf shaped artifact was present, they measured the distance between the middle and the lateral lobes. Otherwise, when an oval shaped artifact was present they measured its greatest dimension.

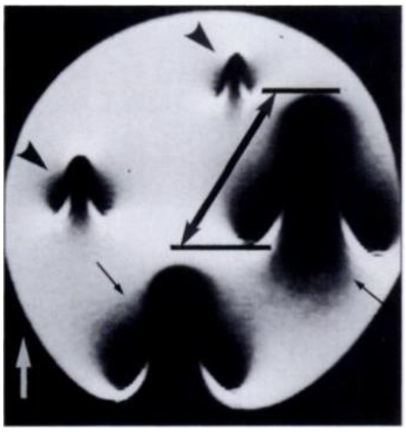

FIG.2:**Measurement of cloverleaf artifact [Adapted from Jin-Suck Suh et 1998].**

In other variations of the observer based method, there is a use of a grid which, is hidden or distorted from the artifact. In these cases distortion margins were estimated as the point at which the grid lines transition from abnormal curvature to a straight orientation ***[Sutherland -Smith et al, 2012]***

Observer studies suffer from intra- and inter-observer variability in artifact in artifact assessment, also affected by digital images viewing conditions, such as window level settings.(see FIG.3)

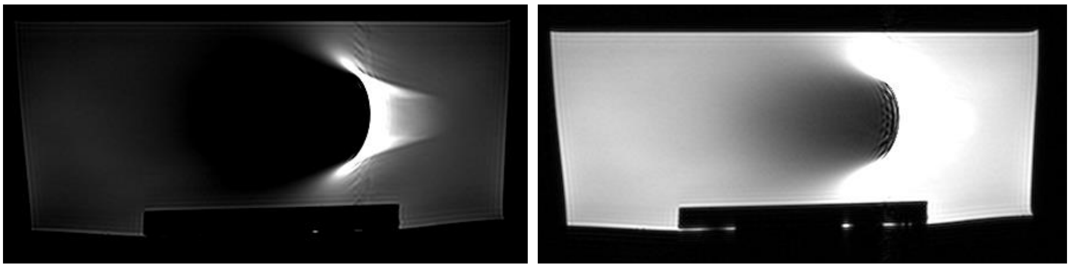

FIG.3 **MR image from the data set analysed. Axial view of a stainless steel Gamma nail acquired at 1.5 T . The two images differ only at the window level settings.**

In FIG.3 the different window setting may provide completely different estimations for the artifact size. Moreover visual observations are hardly reproducible among different observers or different laboratories. The need for more accurate and reproducible measurements have lead to the use of quantitative methods. ***[Matsuura et al.2005]***. They defined a linear region of interest in the center of the biomaterial (cylindrical in shape) in the transverse direction. Then the signal intensity profile was calculated. The same procedure was repeated for a control phantom. A replica of zero magnetic susceptibility artifact was used as control phantom, in order to provide the baseline signal intensity of the surrounding material and the actual implant diameter.

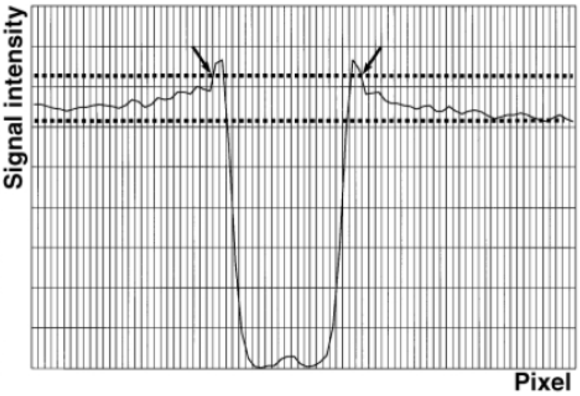

FIG.4: **Signal intensity profile of biomaterial in phantom. The arrows depict the outer borders of the artifact. The region between the two arrows represents the $D_{artifact+implant}$ [Adapted from Matsuura et al, 2005].**

The artifact diameter was defined as the distance between two pixels with signal intensity over mean signal intensity +/- 1.5 SD of baseline intensity (obtained from the control phantom) - Diameter of the implant.

$$D_{artifac} = D_{artifact+implant} - D_{implant}$$

However, sometimes the intensity signal profile in the test and baseline images may be irregular enough making difficult the exact artifact limit determination.

Another approach to metal artifact quantification in magnetic resonance is to consider image regions contaminated by the artifact and thus to consider artifact quantification as an image segmentation problem. This not an easy task since there are not distinct borders. The signal from the artifact may extend in a large range of the gray scale, both in high and in low intensities. Tacheuchi et al ***[Tacheuchi et al, 2011]*** have used a threshold based segmentation method. The used implants embedded in a gel phantom. In order to quantify the borders of the susceptibility magnetic artifacts, the MR images were transformed to bitmap images using a computer software program (imageJ). The authors created a threshold for high intensity artifact and another one for the low intensity artifact. The thresholds are selected in the following way:

The low -signal intensity artifact threshold was defined as the mean value between the mean intensity of the gel phantom and that the lowest value intensity in the low-signal intensity artifacts.

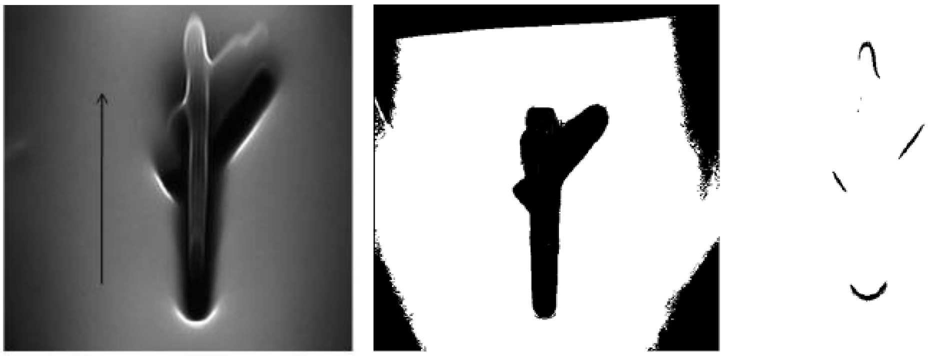

FIG.5: **Image acquired from titanium alloy implant. The bitmap images that follow, correspond to the low intensity and high intensity (misregistration) artifact, after the two thresholds have been applied. The total susceptibility artifact area equals to the sum of the two last images *[Adapted from Tacheuchi et al, 2011].***

The misregistration artifact (high intensity) threshold was defined as the mean value between the gray scale of the gel phantom and that of the highest gray scale in the misregstration artifact. The shade of the misregistration artifact was reversed to black. The sum of low signal intensity area and the high signal intensity area was defined as the total area of the metallic susceptibility artifact.

Port et al ***[Port et al, 2000]*** analyze the images using Scion Image, by auto thresholding the image, converting it into binary and then counting the number of the pixels image in the artifact. In the article there is no any reference to the thresholding method used.

In a recent article ***[Haruki Imai et a,2013]*** uses a visual approach to determine the background intensity and then he creates a 3D artifact model by a simple thresholding technique. First the background intensity is measured. The observer draws two lines along the phase and frequency directions, where the artifact seems to vanish. Then four circular regions of interest 10 mm in diameter, tangential to both lines were positioned where the lines intersected. The background signal intensity was obtained by averaging the signal intensities within the four circular regions. Then they define as artifact any area showing signal intensity that differs more than 30% compared with the average signal intensity. Areas with signal intensity less than 70% or more than 130% of that of the mean background signal intensity is considered as artifact.

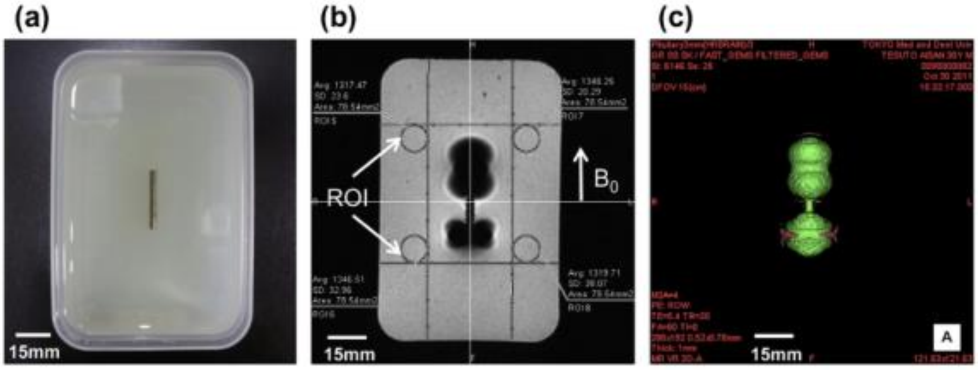

FIG. 6**: (a) the metal implant in gel phantom. (b) MRI acquisition. The vertical lines represent the limits of the artifact free area. The circular ROIs used for background intensity estimation are placed at the intersection of the vertical lines. (c) 3D artifact model.** ***[Adapted from Haruki Imai et a, 2013]***

A very sophisticated algorithm was used by ***[Koff et al, 2013].*** They used a custom phantom, composed of a series of four grid plates. The pattern cut into each grid plate allowed for clear detection of corner points in output images along any plane. The phantom was designed to hold small cylindrical bars of known dimensions made from common orthopaedic hardware materials.

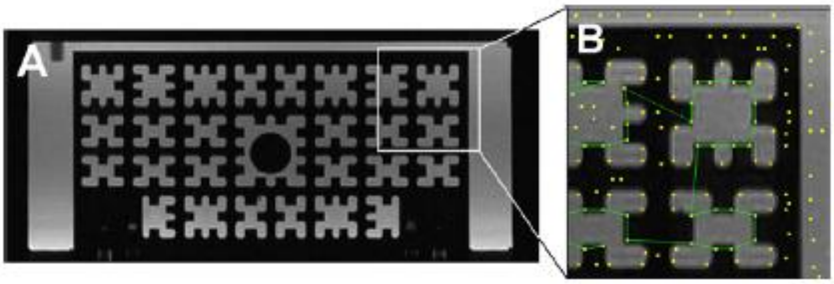

FIG.7:**Edge detection in phantom grid [Adapted from Koff et a 2013]**

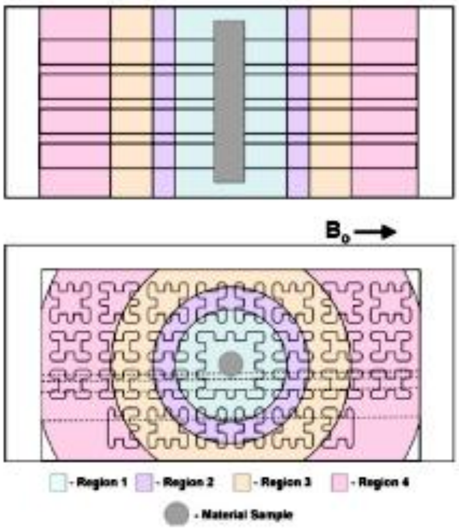

FIG.8: **The four subregions formed in the grid [Adapted from Koff et al 2013].**

A semi - automated program (MATLAB) indentified corners. Then the user manually selects the indentified corners to include in the analysis. The 3D coordinates of the grid corners are calculated. The absolute displacement of the same point in different acquisitions is calculated. The real dimensions of the phantom are already known from the computer aided design. At the coronal images, regional distortion was calculated in four subregions

The four subregions were of radial range, centered at the biomaterial tested. Each subregion contains a number of corner grids, which are either hidden by the artifact, or misplaced due to image distortion.

Since the original dimensions of the grid are already known, the distances differences can be calculated for each sequence or material and then summarized as means and standard deviations. Comparison of the artifact present is carried out through statistical analysis (ANOVA).

A very interesting method of artifact quantification is that described by ***[Kolind et aL.2004]***. In this work a phantom with a wax replica of the real implant, embedded in water is used as a reference. Wax was selected as it is non metallic and has almost the same susceptibility as the water. Every sequence tested, was performed with both the replica and the real implant.

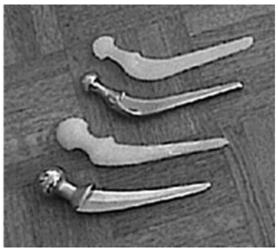

FIG. 9**: Metal orthopaedic implants (hip arthroplasty) and corresponding wax replica [Adapted from *Kolind et aL.2004]*.**

The difference between MR images of the metal phantom and of the wax replica was measured and resolved into contributions from noise, metal artifact and signal. The sum of squares of an MR image can be defined as energy E of the image. Parseval's theorem regarding energy conservation under Fourier transform implies that energy calculations from the image space is equal to the energy in the reciprocal k- space. Another reason that the author prefers to work in the energy field is that noise is a zero mean uncorrelated random field. Only by taking the squares of the pixels we can measure the noise contribution.

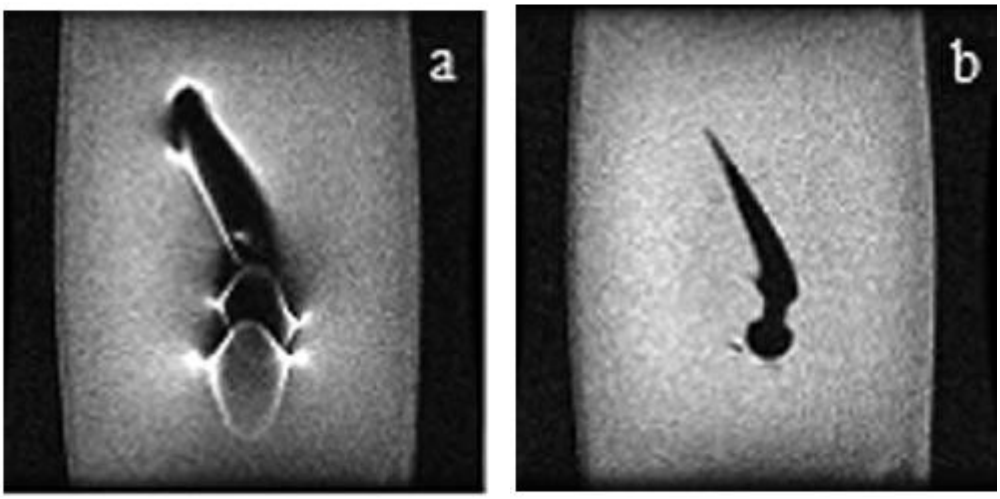

FIG.10: **MR Image acquired from the metal implant (a) and the wax replica(b). The wax replica presents no artifact. Adapted from *[Kolind et aL.2004]*.**

The signal intensities were normalized by dividing an average intensity obtained from four regions . Each slice was normalized separately. The image of the wax prosthesis was then subtracted from that of the metal prostheses, resulting in a map of the difference from the truth. The sum of the squares of the resulting pixels was divided by the total number of pixels to obtain a measure of the total squared difference, or normalized total energy, between the image with artifact and that without. The noise contribution was isolated by performing the same analysis in regions outside of the phantom, in air. Thus, there was no signal and the energy was simply the sum of noise energies of the two images. The noise energy was divided by (2-2π), in order to take into account the difference between the Rayleigh noise distribution in the air and the parent normal noise distribution in water. A measure of the artifact E_A was attained by subtracting the contribution of the noise from the total difference between the images summed over all slices. This last method seems to be the more accurate in the quantification of the artifact. However, although the artifact is quantified, we know nothing about its spatial location. There is no segmentation or thresholding in the image. Moreover for this quantification process reference to a replica of the original implant is always needed.

Although a number of methods, such as the ones described above, have been proposed in the literature to quantify the artifact, there is no consensus about the method of choice. This is attributed both in the difficulty of the task, as well as the dependence of the segmentation methods performance on input parameter value selection. In this frame, this thesis suggests a quantification approach with the following characteristics:

1) It has to be observer independent. The observer should not select region of interest or define any kind of margins in the image

2)It has to be automated and thus easily reproducible

3) It should segment two regions of very different signal intensity in the same image

4) It has to be validated or tested experimentally with a previously reported method, which is considered as state of the art

The method proposed in this thesis ***[Vrachnis et al, 2014]*** fulfills the first three conditions. In order to satisfy the fourth condition we choose to test it with a variation of the energy difference method ***[Kolind et aL.2004]*** described just above. In order to avoid the reference to implant's replica we follow a similar methodology using as reference the image with the lower artifact, instead of an image without artifact at all.

THEORY

Basic MRI principles

Nuclear magnetic imaging is based on the electromagnetic activity of atomic nuclei. Both protons and neutrons have spins. Active nuclei in MRI are considered those having uncoupled spins, since the coupled spins cancel each other out. When an external magnetic field ***H*** is applied the nucleus precess. The precession occurs at a frequency defined by the Larmor equation

$$\omega_0 = \gamma \mathbf{H}$$

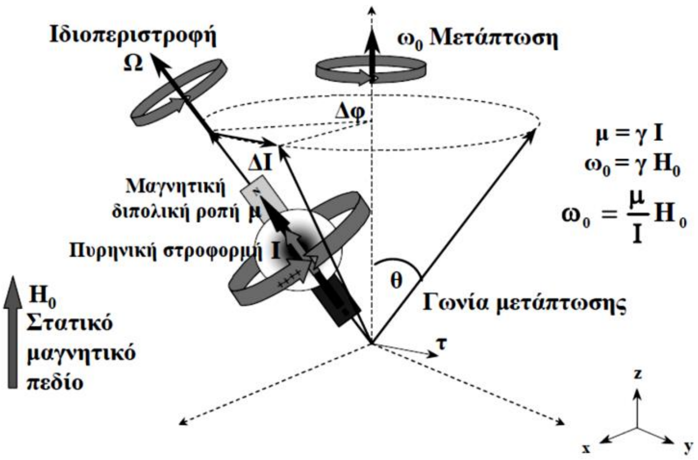

FIG.11:**Precession of nucleus in the presence of external magnetic field H_0. [Adapted from Th Maris " Γενική εισαγωγή στην απεικόνιση μαγνητικού συντονισμού"]**

where ω0 is the precessional frequency, ***H_0*** the applied static magnetic field and γ the gyromagnetic ratio, which is constant for every nucleus at a particular magnetic field strength.

In the absence of external magnetic field the nuclei are oriented randomly . When the external magnetic field is applied they tend to align with the magnetic axis of ***H_0***, some in parallel and others in opposition to it.

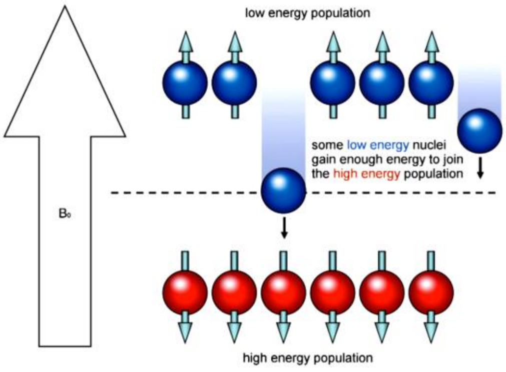

FIG.12: **Energy transfer during excitation [Adapted from Westbrook et al "MRI in practice", 4th edition Wiley-Blackwell, 2011].**

The higher the field strength is the higher the energy difference between this two populations.

The net magnetic moment of the hydrogen nuclei produces a significant magnetic vector, which is called net magnetic vector (NMV). This vector reflects the relative balance between spin up and spin down nuclei.

When an exciting RF pulse at Larmor frequency is applied, the hydrogen nuclei gain energy. The rest nuclei do not resonate since they have different gyromagnetic ratio. Some of the nuclei at the low energy state (parallel to H_0) gain enough energy to join the high energy population. This results in the NMV movement, which aligns away from B_0. The angle that NMV moves out of alignment is called flip angle. The magnitude of flip angle is function of the amplitude and the duration of RF pulse.

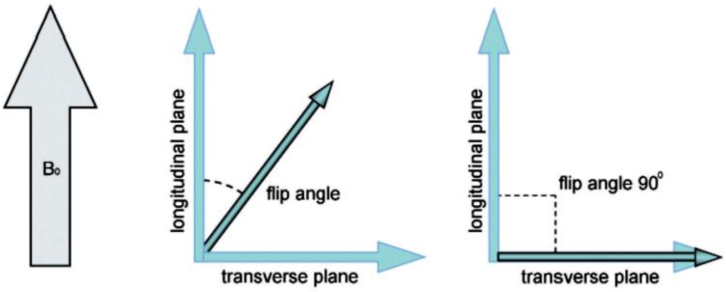

FIG.13: **Flip angle [Adapted from Westbrook et al "MRI in practice" 4th edition Wiley-Blackwell].**

As it can be seen in the above figure, the flip of the NMV produces two magnetization vector components, longitudinal magnetization and transverse magnetization. Only the transverse magnetization vector induces signal in the receiver coil. When the RF energy source is turned off, the net magnetization vector realign with the axis of B_0, through the process of T1 recovery (recovery of the longitudinal vector). Simultaneously the transverse magnetization decreases (decays) through additional mechanism known as T2* decay and T2 decay. Different tissues have different T1, T2, T2* values, which creates the contrast in MRI. Furthermore T2* is dependent on the magnetic environment. The presence of susceptibility variations distorts the magnetic field and affects T2*.

The terms spin-spin and spin lattice interactions have to do with T2 decay and T1 recovery. Spin- spin interactions refer to the interaction of a nucleus with the nearby ones. The movements of the nearby nuclei of hydrogen and paramagnetic atoms result in significant differences in the local magnetic field intensity. This is responsible for high phase loss. Since this interaction is between magnets, which result from the nucleus spin, this kind of interaction is known as spin-spin interaction and represents T2 and T2* decay.

The movements of distant nuclei create changes in the magnetic field. These changes cancel each other out due to the number, the distance and the random of their movement. So these alterations do not contribute to the local magnetic field. However these movements increase the magnetic noise (lattice noise), affecting the number of nuclei in Larmor frequency and in consistency T1.

A pulse sequences is defined as a series of two or more pulses in rapid succession. The free induction decay last only for a few milliseconds after the first pulse, while the slower T1 and T2 continue to exist despite the signal absence. By using only one pulse it is not possible to measure T2 since the FID (free induction decay) contains the T2* decay. This single pulse could only inform as for hydrogen concentration.

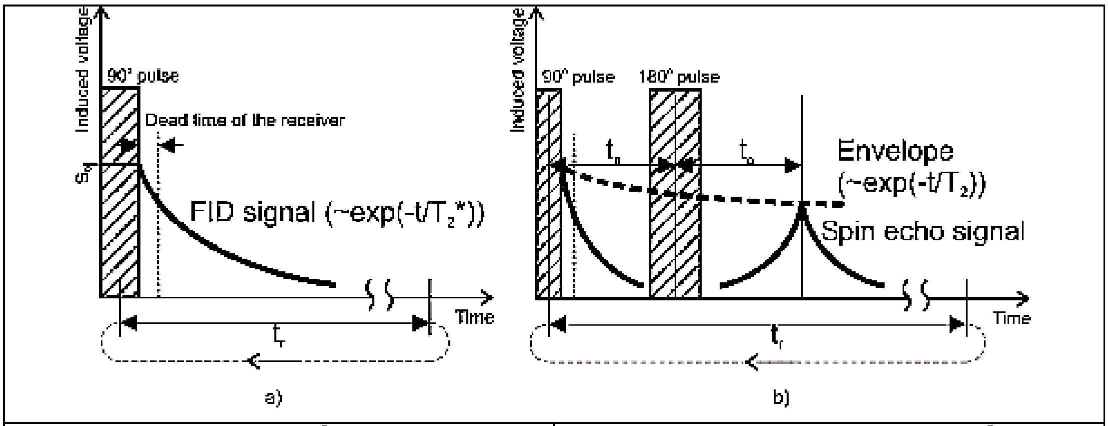

$S = S_0 \cdot [1-\exp(-t_r/T_1)] \cdot \exp(-t/T_2^*)$	$S = S_0 \cdot [1-\exp(-t_r/T_1)] \cdot \exp(-t_e/T_2) \cdot \exp(-t/T_2^*)$

FIG.14: **Free induction decay and T2 decay in Spin Echo sequence [Adapted from http://www.ndt.net/article/ndtce03/papers/v062/v062.htm].**

We use pulse sequences to measure T1 and T2 times, which provide the contrast in MRI. The two major families of pulse sequences are the Spin Echo (SE) and Gradient Echo (GRE). In SE a 90^0 pulse is followed from a 180^0 pulse. When the 180^0 pulse is applied there is no signal. This pulse does not create signal. However signal appears in time equal 2xT (where T is the time from the 90 to 180 pulse) from the 90^0 pulse. This is echo of the initial signal and the 180^0 pulse as a wall in the sonar echo. This pulse is weaker in comparison to the initial signal since it has undergone the T2 decay. By repeating the 180^0 pulse we may take a number of echoes and fit an exponential curve, measuring in this way the T2. TE (time to echo) is the time between the RF pulse and the detection of the first echo.

Measuring T1 is more complicated. In order to measure T1 we have to repeat the whole procedure (the RF and the echoes). the time between the two RF pulses is called time to repetition (TR)

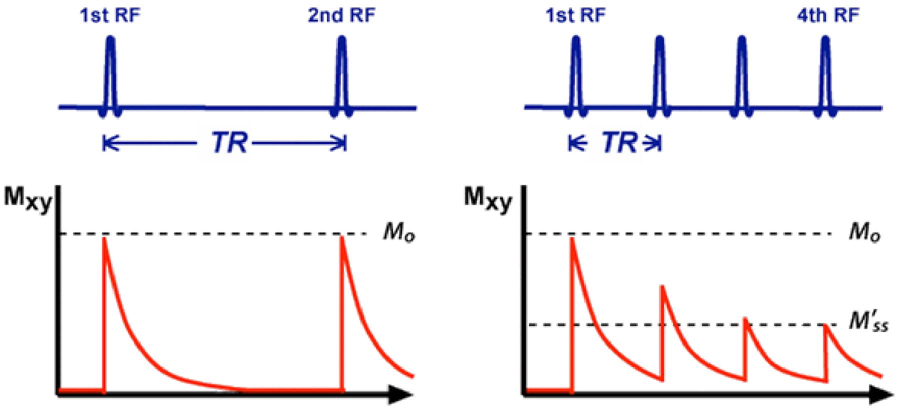

FIG.15: **Free induction decay and TR [Adapted from http://mri-q.com/4-or-more-rf-pulses.html].**

In order to measure T1 (or to give T1 weight in an image), we have to select TR we have to select TR less than T1. The energy loss rate is independent from the phase loss rate. Usually T1>>T2 which means that the energy loss which initiates immediately after the first RF pulse is continued much time after the last echo. When TR<T1 the new RF pulse founds the NMV partially recovered. In this case the vector is not able to absorb all the energy from the new pulse. Consequently both the FID decay and the echoes that result from this second RF pulse are weaker. The T1 exponential recovery of the longitudinal component determines how much weaker is this signal. Again by repeating the procedure as needed and by fitting an exponential we may calculate T1

GRE sequences use gradient reversal instead of RF pulse in order to regenerate the signal. In these sequences. This gradient slows down the fast precessing frequencies and accelerates the slow ones. When all nuclei are in phase, we obtain the maximum signal which is the gradient echo. It is faster than SE since the initial RF pulse does not have to be 90^0 and so the flip angle may be less than 90^0. That means that the recovery time is less. Another advantage is that since there is no other RF pulse than the initial one, the tissue does not get heated. The main disadvantage is that it is very sensitive to field inhomogeneities, such as susceptibility variations, since there is no reversal of the phase loss like in SE equences.

Image acquisition and formation

The signal received from the coil, which consists of many frequencies has to be spatially located in order to form an image. This presupposes a way for selecting the slices to be imaged. All the above are carried out using linear gradients of the magnetic field in the three main axis (x,y,z) when required. This gradients are added to the main static magnetic field.
If we remember the Larmor equation, we will see that the precessional frequency is linear function of the magnetic field intensity.

$$\omega_0 = \gamma \mathrm{B}$$

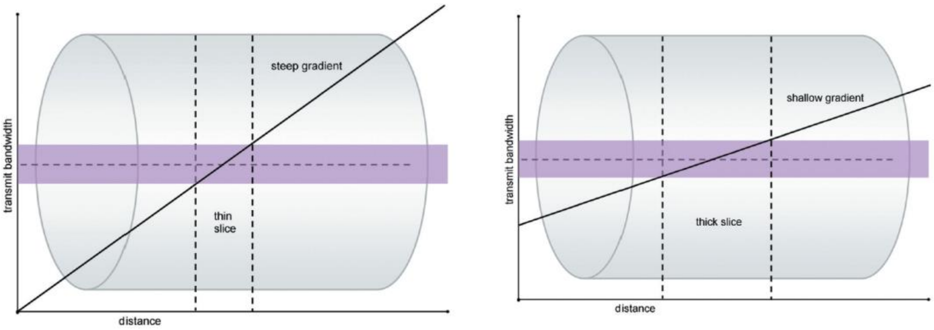

FIG.16: **Slice selection and thickness [Adapted from Westbrook et al "MRI in practice" 4th edition Wiley-Blackwell, 2011].**

The application of the desired gradient (x, y or z) determines the slice plane (z → axial, x → sagittal y→ coronal). The gradient magnitude determines the slice thickness while the central frequency determines it position.

The spatial location of the signal is defined again through gradients. It is encoded through frequency differences in the one axis and through phase differences in the other. The first gradient to apply is the frequency encoding gradient. The basic principle is the same with the slice selection gradient. The spins are located in along the frequency encoding axis according to their frequency as it is related to the encoding gradient through Larmor equation. The encoding occurs simultaneously with the gradient application.
Then the phase encoding gradient is applied for time dt. When the gradient is applied the nuclei located at higher field intensity rotate in higher frequencies. After the phase encoding gradient is switched off, the return to their previous precessional frequency. However due to the previous difference in precessional frequency they obtain phase differences. These phase differences are detected (after the gradient has been switched off) and encode the second axis.(spin -wrap technique)
The data are stored in matrices and their position corresponds to their frequency and phase. This matrix is a spatial frequency space, known as k-space. The data have to undergone Fourier transform in order to give the final image. In each TR a line an k space is completed. The procedure is repeated until the whole k space is completed (there are a lot of ways used to fill k space. Here we refer to the most common one.)

Magnetic properties of materials

Magnetic field

The definitions of magnetism can be described either in terms of circulating currents or in terms of magnetic poles. It is more convenient for our purposes to use the second way.
The force between two magnetic poles is proportional to the product of their pole strength p and inversely proportional to the square of their distance d.

$$F \,\alpha\, \frac{p1p2}{d^2}$$

or in SI unites

$$F = \frac{1}{4\pi\mu}\frac{p1p2}{d^2}$$

In order to explain the interaction between them we can think of the first pole generating a **magnetic field**, ***H*** which exerts a force on the second pole By convention we consider the north pole to be the source of the magnetic field and the south pole to be the sink.

so $H\ a\ \frac{p1}{d^2}$ or $H = \frac{1}{4\pi\mu}\frac{p1}{d^2}$

Another concept related to the magnetic field is the magnetic **Flux**. It is defined as the surface integral of the normal component of the magnetic field. When the flux passes through a unit area perpendicular to the field, it is equal to the field strength.

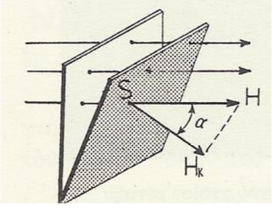

$\Phi =$ **H** A (or $\Phi = \mu_o$ **H** A in SI)

FIG.17:**Magnetic Flux [Προσαρμογή από ΦΥΣΙΚΗ ΤΟΜΟΣ 3 Αλκίνοου Ε.Μάζη, 1963]**

The next concept to introduce is that of the **magnetic moment**. It is referred to the moment exerted on a bar magnet or a current loop when it is inside a magnetic field. Let us introduce a bar magnet, of length l in a magnetic field H at an angle θ.

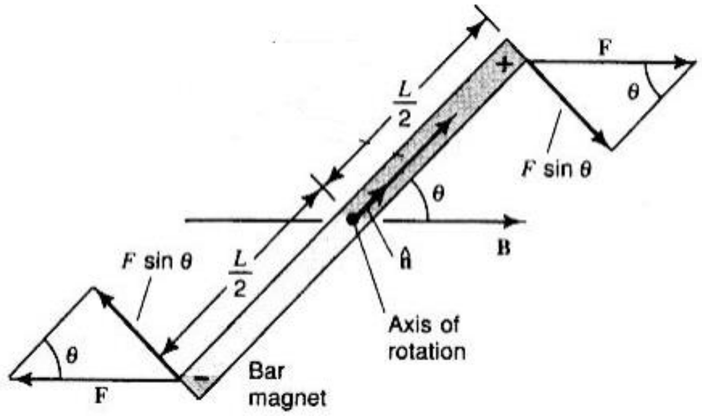

FIG.18:**Bar magnet in magnetic field (adapted from http://homepages.engineering.auckland.ac.nz/~kacprzak/notes.htm)**

The force at each pole **F** =p**H**, where p is the pole strength and **H** the applied magnetic field. The moment acting on the bar will be the external product of the force ***F*** by the distance from the center of mass (equal to l/2)

Thus the moment acting on the magnet is

p ***H*** sinθ $\frac{l}{2}$ + p ***H*** sinθ $\frac{l}{2}$ = pl ***H*** sinθ = m ***H*** sinθ

The m =pl, the product of the magnetic pole by the length of the bar magnet is the magnetic

moment
When talking in terms of current loops the magnetic moment of a current loop of area A that carries current I, thee magnetic moment is defined as the m =I A

Magnetic dipole

The energy of a magnetic dipole is zero by definition when the dipole is perpendicular to the magnetic field.

It can be proven that the energy of a dipole at angle θ to a magnetic field is $E = -mH\cos\theta$
$= -\boldsymbol{mH}$
or $E = -\mu_o \boldsymbol{mH}$ in SI units

Magnetization

We define as **magnetic induction *B*** the response of a material after the application of a magnetic field ***H.*** The relationship between ***B*** and ***H*** is a property of the material. In free space and in some materials it is usually a linear relation. However it is not always the case.

$$\boldsymbol{B} = \boldsymbol{H} + 4\pi\boldsymbol{M}$$

or

$$\boldsymbol{B} = \mu_o(\boldsymbol{H} + \boldsymbol{M}) \text{ in SI units,}$$

where μ_0 is the permeability of the free space

The M introduced above is the **magnetization** of the medium and it is defined to be the magnetic moment per unit volume

$$\boldsymbol{M} = \frac{\mathbf{m}}{\mathrm{V}}$$

Magnetization is property of the material and it depends on the magnetic moments of its ions or molecules and the way they interact .

The magnetic induction ***B*** inside the material is the same thing as the density of the flux Φ inside the material. In other words inside the material $\boldsymbol{B} = \frac{\Phi}{A}$. In free space $H = \frac{\Phi}{A}$

We can classify the materials according to the internal and external flux when placed in a magnetic field
Materials where the magnetic flux Φ inside is less than outside are known as diamagnetic. When the magnetic flux inside is slightly higher than outside is categorized as either

paramagnetic or antiferromagnetic. Finally in those where flux inside is much greater than outside, the material is characterized either ferromagnetic or ferrimagnetic.
The details of these classification are discussed later.

Susceptibility and permeability

Susceptibility χ is introduced in order to show how responsive is a material in an applied magnetic field. It is defined as the ratio of ***M*** to ***H***

$$\chi = \frac{\boldsymbol{M}}{\boldsymbol{H}}$$

As permeability μ the ratio of ***B*** to ***H*** is defined

$$\mu = \frac{\boldsymbol{B}}{\boldsymbol{H}}$$

Since $\boldsymbol{B} = \mu_0 (\boldsymbol{H} + \boldsymbol{M})$

$$\frac{\mu}{\mu_0} = 1 + \chi$$

Diamagnetism

Diamagnetism is due to change in the orbital motion of electrons when an external magnetic field is applied. It is a phenomenon occurring in all atoms. The underlying principle is Lenz's law. When the magnetic field is turned on extra currents are generating in the atom through magnetic induction. The currents induced have such a direction, that tends to invert the initial cause. In other words the magnetic moments are directed opposite to the applied field. Diamagnetism is a weak phenomenon and in many atoms is not observed because stronger interactions outshine it.
Langevin theory gives as an expression for the diamagnetism, explaining the negative susceptibility in terms of motion of electrons (classical derivation - the quantum mechanical derivation gives the same results)

We consider an electron orbiting perpendicular to a magnetic field. It creates a current with opposite direction to its motion. When we switch on the magnetic field, according to Lenz's law, an electromotive force ε which tends to oppose the change in flux, is induced.

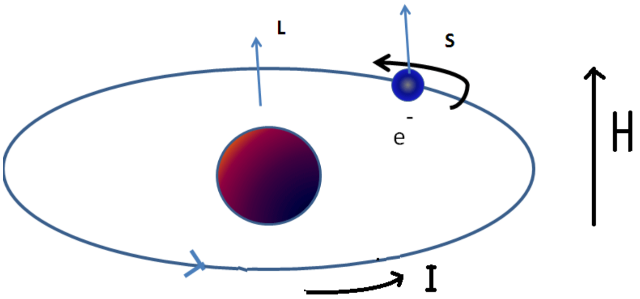

FIG.19: **Orbiting electron perpendicular to magnetic field H (adapted and altered from http://www.reddit.com/r/Elements/comments/g9op9/magnetism_and_magnets_part_2_filling_orbitals/)**

The electromotive force is the line integral of the electric field E around a close path. If we consider the electron orbit radius r, then the path equals 2πr and the electromotive force is equal to Ex2πr. According to Faraday's law it is also equal to the rate of change of the magnetic flux through the path $-\frac{d\Phi}{dt}$

$$\text{So } \varepsilon = \text{E}\times 2\pi\text{r} = -\frac{d\Phi}{dt} \quad (1)$$

The change in flux is achieved by reducing the electron velocity and thus the current circulating in the loop. That means that the magnetic moment of the loop is also decreased and that is what we observe as diamagnetic effect. The electromotive force acts as long as there is change in the magnetic flux. However the alteration in the electrons velocity remains since there in no force acting to drive it to its previous velocity. So the diamagnetic effect lasts al long as the field is acting

The torque exerted on the electron buy the induced magnetic field is ***F***r = -eEr.
The rate of change of the angular momentum is equal to the torque exerted on the electron

$$\text{So } \frac{dL}{dt} = -\text{eEr} \quad (2)$$

In general, $\Phi = \mu_o HA$ (3), where in our case $A = \pi r^2$. We take $\mu = \mu_0$ because we consider a free atom.
Combining all the above equations (1), (2), (3) we take

$$\frac{dL}{dt} = -\text{eEr} = +\frac{e}{2\pi}\frac{d\Phi}{dt} = \frac{er^2\mu_0}{2}\frac{dH}{dt}$$

If we integrate, considering that the initial magnetic field is zero, we take

$$\Delta L = \frac{er^2\mu_0}{2}\boldsymbol{H}$$

The additional angular momentum makes an extra magnetic moment
Since $L = m_e ur$ and $I = -\frac{eu}{2\pi r}$

then m = IA $= -\frac{e}{2m_e}L \Rightarrow \Delta m = -\frac{e}{2m_e}\Delta L \Rightarrow$

$$\Delta \boldsymbol{m} = -\frac{e^2 r^2 \mu_0}{4m_e}\boldsymbol{H}$$

in other words the derived magnetic field is proportional to the magnetic field and in the opposite direction to it.

The above formula is valid for an electron perpendicular to the magnetic field. Because in classical description all orientations are allowed, which means other than perpendicular the effective magnetic moment is reduced by a factor 2/3. Taking in account the contribution

from electrons from different orbitals to diamagnetism, the previous formula is transformed to

$$\Delta \boldsymbol{m} = -\frac{Ze^2 r^2 \mu_0}{6m_e}\boldsymbol{H}$$

In order to convert to a volume magnetization we multiply by N, which is the number of atoms per unit volume.

As we have seen earlier, magnetic susceptibility is defined as $\chi = \frac{M}{H}$

thus

$$\chi = -N\frac{Ze^2 r^2 \mu_0}{6m_e}$$

Diamagnetic susceptibility is always negative and it is temperature independent (it is altered to the degree that orbital radius change with the temperature)

Diamagnetism meats magnetic resonance imaging and from the point of the superconductivity, since the superconductors are diamagnets, and below their critical temperature are perfect diamagnets with susceptibility of -1

Paramagnetism

While diamagnetic effect, which is present in all materials, is dominant in those with no net magnetic moment, paramagnetism is observed in materials with net magnetic moment. The magnetic moments of the are randomly aligned, due to thermal motion. The application of an external magnetic field, tends to align a small portion of them to the direction of the field. As paramagnetics are categorized many transition metal salts (as a result of the unfilled d shell), rare earth salts (due to high localized f electrons that do not overlap with f electrons on adjacent ions), some metals (like aluminum) or gases (like oxygen). More over all ferromagnetic materials above a critical temperature (Curie temperature) are converted to paramagnetics due to thermal motion.

Talking for low fields, susceptibility is constant (χ = M/H). It takes values between 10^{-3} and 10^{-5}. That means susceptibility is slightly higher than zero and permeability slightly greater than one

Two theories have been developed in order to explain the effect. Langevin theory for paramagnetism and Pauli paramagnetism

Langevin Theory for paramagnetism

Langevin explains the temperature dependence of susceptibility in paramagnetics. We assume non interacting magnetic moments arranged randomly due to thermal motion. The application of a magnetic field tends to shift their orientation towards the magnetic field. According to Boltzmann statistics or a moment which at angle θ to the magnetic field ***H*** the probability of being in an energy state E is

$$e^{-E/K_BT} = e^{mHcos\theta/K_BT}$$

where m, H the magnetic moment and field. The number of magnetic moments lying between angles θ and dθ is proportional to the surface area of a surrounding sphere. The elementary area we consider is $dA = 2\pi r^2 \sin\theta d\theta$

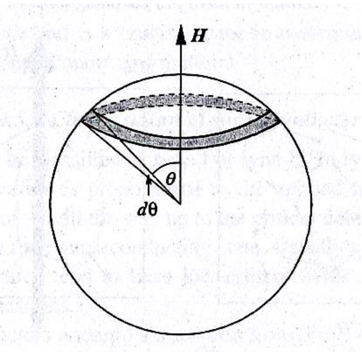

FIG.20:**Fraction of paramagnetic moments between angles θ and dθ, around an axis. Adapted from "Magnetic materials. Fundamentals and device applications" N Spaldin, Cambridge University Press 2003**

The probability of an atomic moment to be between θ and dθ is

$$p(\theta) = \frac{e^{mHcos\theta/K_BT} sin\theta d\theta}{\int_0^{\pi} e^{mHcos\theta/K_BT} sin\theta d\theta}$$

Taking in consideration each moment contribution which is parallel to the magnetic field equal to mcosθ ,the total magnetization ***M*** equals to:

$$\boldsymbol{M} = \mathrm{N}\boldsymbol{m}(\cos\theta)$$
$$= \mathrm{N}\boldsymbol{m}\int_{\mathbf{0}}^{\boldsymbol{\pi}} \cos\theta \, p(\theta) d\theta$$
$$= \mathrm{N}\boldsymbol{m}\frac{\int_0^{\pi} \; e^{mHcos\theta/K_BT} cos\theta sin\theta d\theta}{\int_0^{\pi} e^{mHcos\theta/K_BT} sin\theta d\theta}$$

After making all the necessary calculations, we take

$$\mathrm{M} = \mathrm{Nm}\left[\coth\left(\frac{mH}{K_B T}\right) - \frac{k_B T}{mH}\right]$$

We name $\alpha = \frac{mH}{K_B T}$ and L(α) =cothα - 1/α (Langevin function)

Then

$$\boldsymbol{M} = \mathrm{N}\boldsymbol{m}\,\mathrm{L}(\alpha)$$

That means that there is absolute alignment of the moments if we make α large enough either by using high magnetic fields or by lowering the temperature towards absolute zero, (since then $\boldsymbol{M} = \mathrm{N}\boldsymbol{m}$)

By expanding Langevin's function at Taylor series ***M*** equals to

$$\boldsymbol{M} = \frac{Nm^2}{3k_B}\frac{\boldsymbol{H}}{\mathrm{T}}$$

and the susceptibility $\chi = \frac{M}{H} = \frac{Nm^2}{3k_B}\frac{\mathbf{1}}{\mathrm{T}}$

This is Curie's law, susceptibility of a paramagnetic is inversely proportional to the temperature, since $\frac{Nm^2}{3k_B}$ is constant.

The same is true if we take in consideration quantum limitations for discrete orientations of the magnetic moment (Brillouin function)

Again susceptibility is inversely proportional to temperature

Curie law derives, by supposing no interaction between atomic magnetic moments. However many paramagnetics do not obey exactly Curie's law, although they saw some temperature dependence. Weiss explained this "abnormality" by introducing the concept of "molecular field" which represents the internal interaction between localized moments (mean field theory).

He made the assumption that the intensity of the molecular field is propotional to the magnetization , so

$$\boldsymbol{H}_w = \gamma \boldsymbol{M}$$

where γ is the molecular field constant

Then

$$\boldsymbol{H}_{tot} = \boldsymbol{H}_w + \boldsymbol{H}$$

From Curie law we know that

$$\chi = \frac{\mathbf{M}}{H} = \frac{C}{T}, \text{ where C stands for constant}$$

Weiss replaced the ***H*** of Curie's law with $\boldsymbol{H}_{tot} = \boldsymbol{H}_w + \boldsymbol{H}$ and thus

$$\boldsymbol{M} = \frac{C\boldsymbol{H}}{T - C\gamma}$$

or

$$\chi = \frac{M}{H} = \frac{C}{T-\theta}$$

When T =θ, there is the transition from paramagnetic to ferromagnetic. That means that the "molecular field" acts in the same direction with the applied field and tends to make the magnetic moments to align parallel to each other and to the applied field
C is constant specific for the material, and θ is the Weiss constant (which is somewhat higher from the actual Curie temperature)

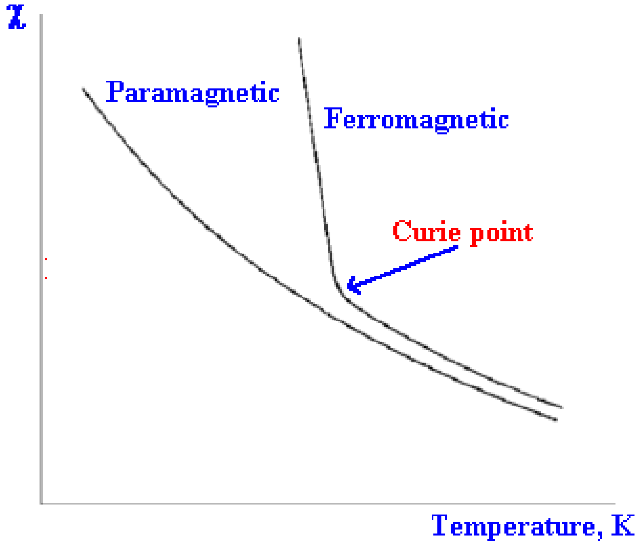

FIG.21: **Susceptibility vs temperature. Below the critical Curie temperature the paramagnetics become ferromagnetic [Adapted from http://wwwchem.uwimona.edu.jm/courses/magnetism.html].**

Pauli paramagnetism

Langevin's theory on paramagnetism fails in the case of metals, where the susceptibility seems to be independent of temperature. It is well known that in metals electrons are able to move freely through the lattice. When atoms approach to form a solid, the waveforms of the outermost valence electrons overlap. The result is the formation of bands.
The electrons in solids (and in free atoms as well) occupy the energy bands with the lowest energy fisrt. The highest energy level is filled at the absolute zero. The energy of this level is called Fermi energy E_F. In paramagnetic metals the energy states for up and down spins of the electrons is the same. This is true and for the Fermi energy level. However, when an external magnetic field is applied the spins that are aligned parallel to the magnetic field have lower energy than those which are antiparallel. So they tend to align themselves parallel to the magnetic field. However the exclusion principle of Pauli, does not allow two electrons to have all the quantic numbers the same. The only way to reorient parallel to the magnetic field is to move in a vacant parallel moment state. Electrons close to the Fermi energy level have the energy required to do this.
By applying Schrödinger's equation for free electrrons, we can calculate the number of electronic states per electron energy at the Fermi level. It is

$$D(E_F) = \frac{V}{2\pi^2}\left(\frac{2m_e}{\hbar^2}\right)^{3/2} E_F^{1/2}$$

or by substituting $\frac{V}{3\pi^2}\left(\frac{2m_e}{\hbar^2}\right)^{3/2}$ by $\left(\frac{N}{E_F}\right)^{3/2}$

$$D(E_F) = \frac{3}{2}\frac{N}{E_F}$$

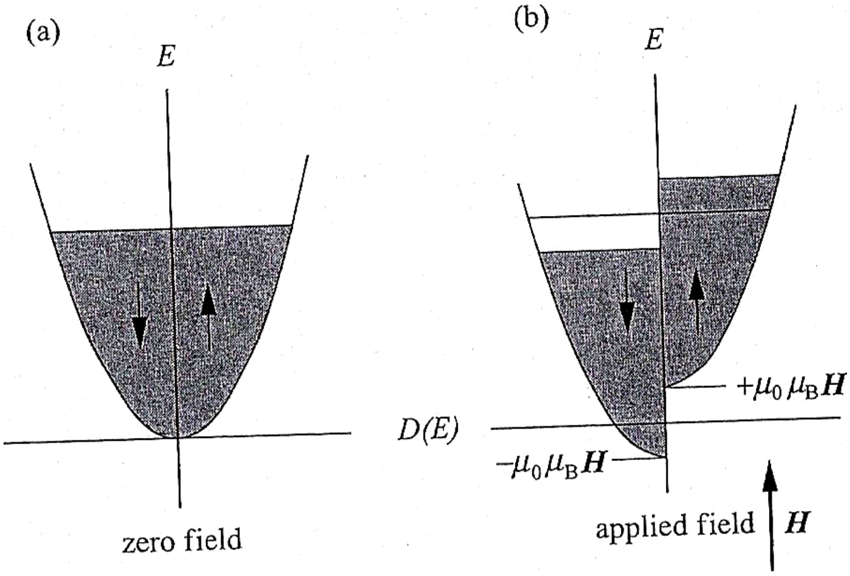

FIG.22: (a)Density of states in a free electron gas with no applied field. The up and down spin densities of states are equal and proportional to the square root of energy
(b) Energy of states in a free electron gas when magnetic fielf is applied in the up direction. The down spin states which have up magnetic moments, are lowerd in energy and the up spin states are raised in energy [Adapted from "Magnetic materials. Fundamentals and device applications" N Spaldin,2003)]

When a magnetic field is applied, an electron which has its magnetic moment aligned with the magnetic field lowers its energy by an amount $\mu_0\mu_B\boldsymbol{H}$, while electrons with opposite spin raise their energy at the same amount ($\mu_B = \frac{e\hbar}{2m_e}$, Bohr's magneton)
The net magnetic moment is the number of down-spins minus the number of up-spins .
After the necessary calculations

$$\boldsymbol{M} = \mu_0\mu_B{}^2\boldsymbol{H}\, D(E_F)$$

or by replacing $D(E_F) = \frac{3}{2}\frac{N}{E_F}$ and since $\chi = \frac{\boldsymbol{M}}{\boldsymbol{H}}$=>

$$\chi = \frac{3N\mu_0\mu_B{}^2}{2E_F}$$

Diamagnetic contribution is found to be 1/3 of Pauli paramagnetism, so the total susceptibility is $\chi = \frac{N\mu_0\mu_B{}^2}{E_F}$

Ferromagnetism

If we study the change of magnetization in relation to the applied magnetic field, for ferromagnetic materials we make some very interesting observations. First we observe that small external fields create large magnetization. Moreover, above a certain external field strength the magnetization saturates. (FIG.23)

In addition, when the magnetic field is removed, the magnetization does not reduce to zero, a phenomenon known as hysteresis. The graph of ***B*** (or ***M***) versus ***H*** , called hysteresis loop, is used to describe the effect.

The material starts at zero field and at zero magnetization. B_s is called the saturation induction and it corresponds to the magnetization saturation. The part of the curve from demagnetized state to the saturation induction is called normal induction curve. Additional increase in the magnetic field does not increase the magnetization. However, the B increases since, $\boldsymbol{B} = \boldsymbol{H}+4\pi\boldsymbol{M}$. When the magnetic field is removed, the magnetization decreases to what is known as residual induction or retentivity B_r. Then, in order to reduce the induction to zero, a reversed field is required. The value of the field required to reduce the induction to zero since it is magnetized is called coercivity $\boldsymbol{H_c}$. The value of $\boldsymbol{H_c}$ is used to categorize the ferromagnetic materials as hard or soft. Hard means that it has large $\boldsymbol{H_c}$ or it needs large field to saturate the magnetization, while soft materials are both easily magnetized and demagnetized.

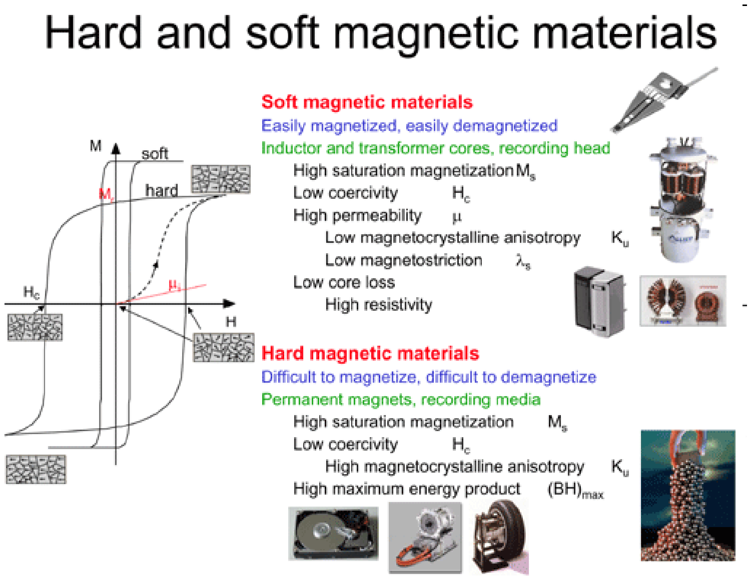
Hard and soft magnetic materials

Soft magnetic materials
Easily magnetized, easily demagnetized
Inductor and transformer cores, recording head
- High saturation magnetization M_s
- Low coercivity H_c
- High permeability μ
  - Low magnetocrystalline anisotropy K_u
  - Low magnetostriction λ_s
- Low core loss
  - High resistivity

Hard magnetic materials
Difficult to magnetize, difficult to demagnetize
Permanent magnets, recording media
- High saturation magnetization M_s
- Low coercivity H_c
  - High magnetocrystalline anisotropy K_u
- High maximum energy product $(BH)_{max}$

FIG.23: **Hysteresis loop of soft and hard ferromagnetic materials [Adapted from http://www.nims.go.jp/apfim/soft&hard.html]**

The first successful attempt to explain the properties of ferromagnetic materials was the domain theory of Weiss. Weiss already knew from Curie-Weiss law, that ferromagnetic materials become paramagnetic above Curie temperature. That led Weiss to assume that as in the case of paramagnetic materials, there is also a molecular field strong enough to maintain the magnetization in the absence of an external magnetic field.

As we have seen earlier from Langevin's theory of paramagnetism

$$\boldsymbol{M} = N\boldsymbol{m}\, L(\alpha) \ (1)$$

where $\alpha = \frac{mH}{K_B T}$ and $L(\alpha) = \coth\alpha - 1/\alpha$

The contribution of the molecular field to the magnetization is $\boldsymbol{M} = \frac{\boldsymbol{H_w}}{\gamma}$ (2)with γ being the molecular field constant.

If we plot together the (1) and (2), we observe two intersection points, one at the origin and one at the point corresponding to the smallest spontaneous magnetization

fig6.1

When no external field is applied, the total ***H*** is provided by the molecular field. So $H=H_w$.

From the equations above:

$$\alpha = \frac{mH}{K_B T} = \frac{mH_w}{K_B T} = \frac{m\gamma M}{K_B T} \text{ or}$$

$$M = \left(\frac{K_B T}{\boldsymbol{m}\gamma}\right)\alpha$$

Magnetization is linear function of a. The slope is proportional to temperature. The tangent at the origin represents the slope for $T = T_C$. These means that above this temperature, no spontaneous magnetization occurs.

The combination of Langevin and Weiss theories describes many properties of ferromagnetic and paramagnetic material. However fails to explain some experimental observations. The first observation which cannot be explained by Weiss theory, is the fact that the magnetic dipole moment is not the same in the ferromagnetic and paramagnetic phase (Weiss theory suggests that they should be the same). The second experimental observation has to do with the Langevin theory. The localized -moment theory proposed by Langevin implies that the magnetic dipole moment should correspond to an integer number of electrons. However experimental data show the opposite

According to classical electromagnetism, two nearby magnetic dipoles tend to align in opposite directions. In few materials a strongest interaction is developed. This is known as exchange interaction. It is related to Pauli exclusion principle, which does not allow two electrons to have all quantum numbers the same. They can occupy the same position only if they differ in the spin. The exchange interaction arises from the electrostatic repulsion between electrons. It is much stronger than the magnetic dipole-dipole interaction and can lead change in spin. Under certain conditions when the orbitals of unpaired outer electrons from adjacent atoms overlap, their electric charge is distributed further apart when the electrons have the same spin than when they have opposite spin. The electrostatic repulsion is reduced. In the elementary ferromagnetic transition metals (Fe, Ni, Co), the Fermi energy lies in a region of the overlapping 3d and 4s bands. As a result of this overlapping the valence electrons partially occupy the 3d and 4s band (more the 3s and less the 4d). The 4d band is broad with low density of states at the Fermi level. The energy which would be required to promote a 4s electron to a vacant state is so that it could reverse its spin is more than which would be gained by the resulting increase in the exchange energy. By contrast the 3d band is narrow and has much higher density of states at the Fermi level. The large number of electrons near the Fermi level reduces the energy required to reverse a spin and the exchange effect dominates. The exchange interaction causes the change in energy and an external field is not required to induce magnetization.

MRI compatibility

As we have shown magnetization is a function of the applied field and the inherent magnetization M_0 some materials have even in the absence of an external magnetic field.

So $\boldsymbol{M} = \boldsymbol{M_0} + \chi \boldsymbol{H}$

The term $\chi\boldsymbol{H}$ accounts for the external field induced magnetization. In most cases the induced magnetization is a linear function of the applied external field, as in the equation above. However, in large fields, the magnetization may vary proportional to quadratic cubic or higher power of $\boldsymbol{H}$. In MRI the linear approximation suffices.

In terms of magnetic properties the materials are three categories: Hard magnetic, soft magnetic and non magnetic materials. The hard magnetic materials have non zero permanent magnetization, which may vary from nearly zero as 10^6A/m for some alloys. It is not truly constant, but it depends on previous exposure on magnetic field. Field induced changes in M_0 persist to some degree when the magnetizing field is removed. Magnetic hardness is defined as the ability to resist field induced changes in M_0 and to maintain high remnant magnetization.

Soft magnetic materials are not magnetized unless they are subjected to an applied magnetic field. Their susceptibility is large and they exhibit easily detected torques and forces in presence of strong magnetic field. In non magnetic materials no forces or torques are detected when they are placed in an applied field. However field induced magnetization can be demonstrated by use of proper sensing equipment. There is no precise susceptibility value separating soft magnetic from non magnetic materials. However materials with non zero M_0 or with susceptibility greater than 0.01 may be classified as magnetic materials. Hard or soft magnetic materials are considered MRI incompatible

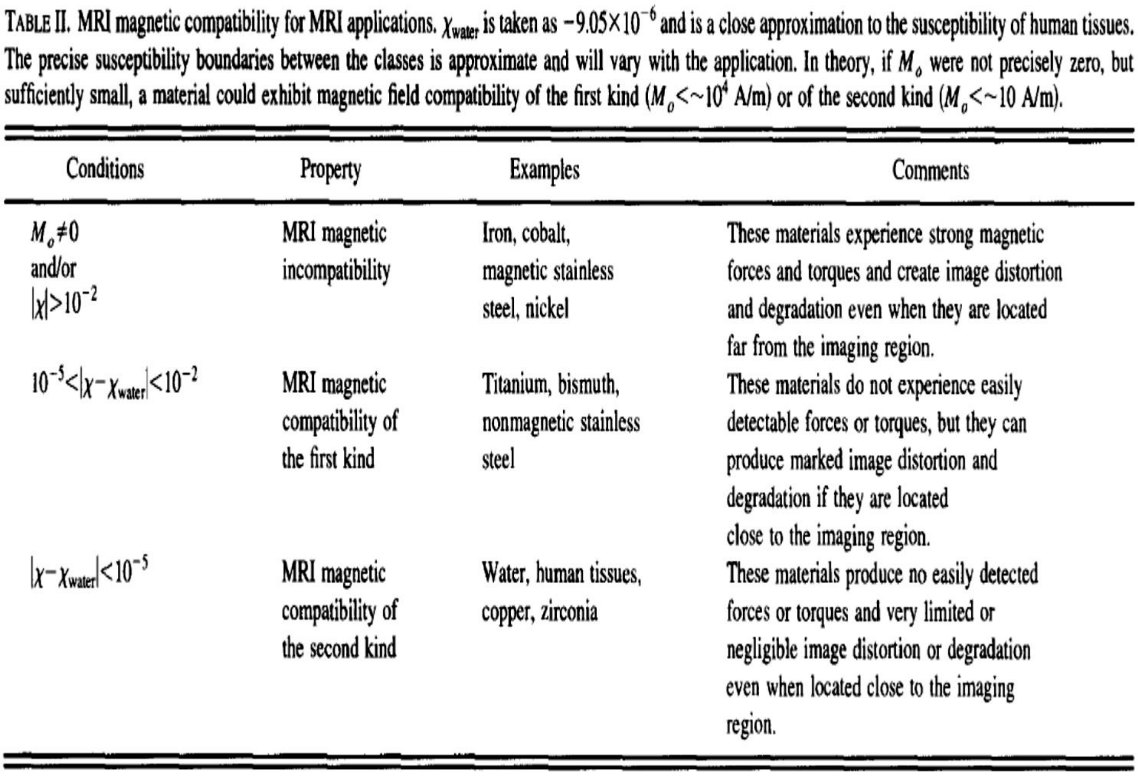

TABLE II. MRI magnetic compatibility for MRI applications. χ_{water} is taken as -9.05×10^{-6} and is a close approximation to the susceptibility of human tissues. The precise susceptibility boundaries between the classes is approximate and will vary with the application. In theory, if M_0 were not precisely zero, but sufficiently small, a material could exhibit magnetic field compatibility of the first kind ($M_0 < \sim 10^4$ A/m) or of the second kind ($M_0 < \sim 10$ A/m).

Conditions	Property	Examples	Comments
$M_0 \neq 0$ and/or $\lvert\chi\rvert > 10^{-2}$	MRI magnetic incompatibility	Iron, cobalt, magnetic stainless steel, nickel	These materials experience strong magnetic forces and torques and create image distortion and degradation even when they are located far from the imaging region.
$10^{-5} < \lvert\chi - \chi_{water}\rvert < 10^{-2}$	MRI magnetic compatibility of the first kind	Titanium, bismuth, nonmagnetic stainless steel	These materials do not experience easily detectable forces or torques, but they can produce marked image distortion and degradation if they are located close to the imaging region.
$\lvert\chi - \chi_{water}\rvert < 10^{-5}$	MRI magnetic compatibility of the second kind	Water, human tissues, copper, zirconia	These materials produce no easily detected forces or torques and very limited or negligible image distortion or degradation even when located close to the imaging region.

TABLE 1: **Magnetic compatibility for MRI applications [Adapted from John F.Schennck: "Role of magnetic susceptibility in MRI", 1996]**

The non magnetic material exhibit a continuous range of magnetic properties. In the table above (John F.Schennck) , for simplicity reasons the nom magnetic materials are classified in to MR compatibility books of the first and second kind. The susceptibility of the materials of the *first kind* have susceptibility large enough to degrade the image, when they are present or in the vicinity of the imaging region.

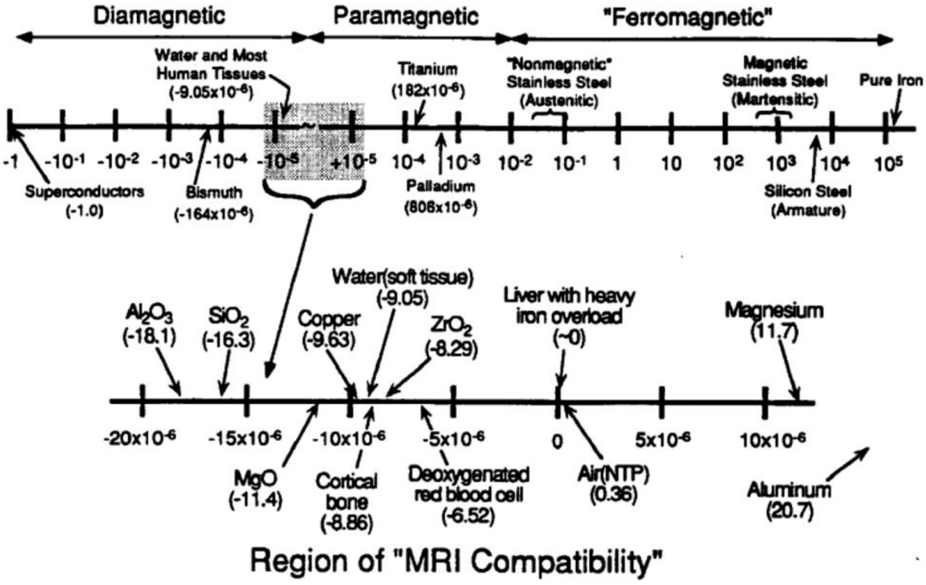

FIG.24: **Susceptibility spectrum [Adapted from John F.Schennck "Role of magnetic susceptibility in MRI",1996]**

Mechanical forces are not detected in these materials. The group of magnetic compatibility of the second kind, includes materials with magnetic susceptibility close to that of human tissues and no artifact is induced.

Mechanism of susceptibility artifact generation

***As image artifact (or artefact) is defined any feature appearing in the image that does not exist in the imaged object*.**

The introduction of any object in the magnetic field induces changes in the magnetic flux density. When placed in an homogenous magnetic field the object produces inhomogeneities in the local magnetic field that interfere with the imaging gradient. The resulting image distortions, which are what we call magnetic susceptibility artifacts, are more marked when the differences in the magnetic susceptibilities between the object and the surrounding matter are substantial. The resulting distortions alter the phase and the frequency of local hydrogen nucleus spin. These alterations in the nucleus spin result in an erroneous proton nucleus location in image matrix due to image distortion in slice selection (through plane distortion) and due to frequency encoding failure (in plane distortion)

Through plane distortion

When a gradient coil is switched on, the magnetic field strength, and the precessional frequency of nuclei located along its axis, is altered in a linear fashion. A specific point long the axis of the gradient has a specific precessional frequency

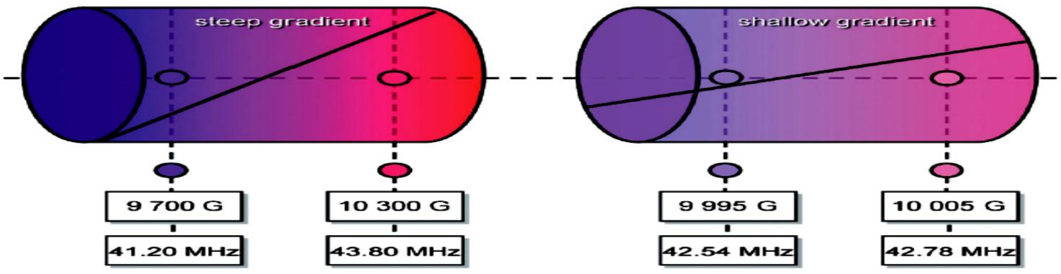

FIG.25: **MRI gradient [Adopted from "MRI in practice"]**

Nuclei situated within a slice have a specific prrecessional frequency. A slice can be selectively excited by transmitting RF with a band of frequencies coinciding with the Larmor frequencies of spins in the particular slice as defined by the slice select gradient. Nuclei situated in other slices along the gradient do not resonate, because their precessional frequency is different due to the presence of the gradient. The scan plane selected determines which of the three gradients is used to make the slice selection. Thus z gradient alters the field strength along the z axis and it is used to select axial slices, while in similar manner, the x and y gradient select sagittal and coronal slices respectively. In the absence of field inhomogeneities the mapping between spin's precession frequency and its spatial location is linear function (see dotted line in the figure below). When metal induced inhomogeneities superimpose upon slice selection gradient , the resulting frequency - position mapping becomes highly non linear (solid line in the figure below), which causes problems in slice selective excitation and frequency encoding during readout.

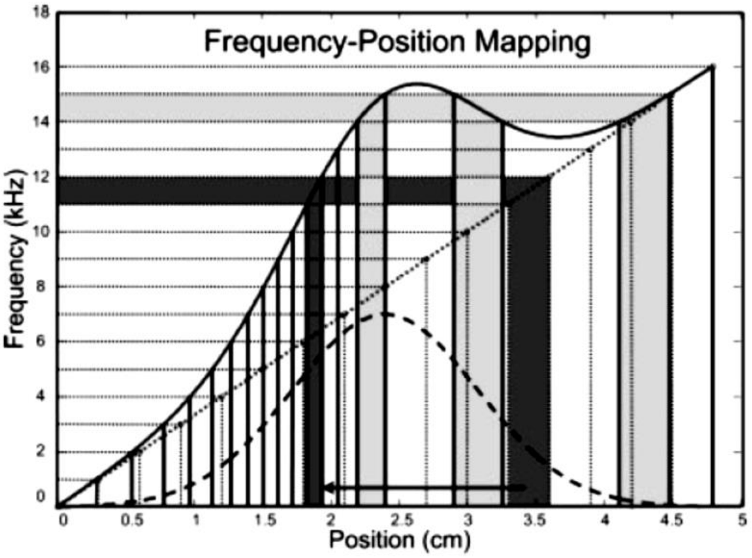

FIG.26: **Frequency position mapping in the presence (solid line) and in absence (dotted line) of field inhomogeneities [Adapted Wenmiao Lu et al 2009]**

As illustrated in the figure above, an RF pulse with 1 KHz bandwidth centered at 11.5 KHz is designed to excite a 3mm thick slice, centered at location 3.3 cm However because of the non linear frequency position mapping, the RF pulse, excites a thinner slice centered at 1.8cm. This results in through plane distortion and in signal loss due to thinner slice. Another RF pulse 1KHz centered at 14.5 KHz excites spins centered around three locations (2.3, 3.1 and 4.1cm depicted in the figure above as light gray regions).

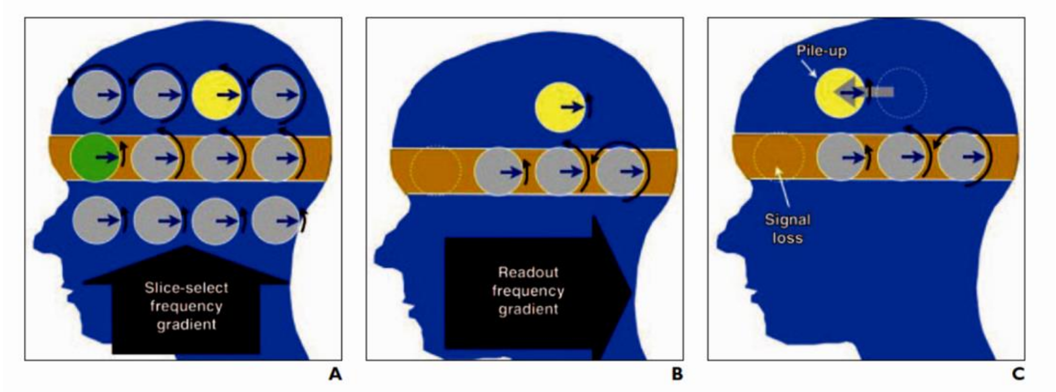

FIG.27: **(A).Yellow and green spins resonate below expected resonant frequency during slice selection. When Rf pulse is centered at rate of gray spins in orange region, green spin is not excited while yellow spin is. This results in signal loss (green) and signal pile up (yellow).**
(B)When spins are imaged (readout gradient) will again resonate below expected rate and are detects at incorrect position
(C)The result is in plane pill up artifact.
[Adapted from Hargreaves et al, 2011].

These errors can cause a shift in the excited slice, or curving (potato chip effect). It can cause the slice to be thicker or thinner than desired and can even result in splitting of the slice into multiple regions. The overall result is that the selected slice differs from what the desired. The initially desired slice portion no longer represents the location of the image. Thinning and thickening lead to clear signal loss or pile ups.

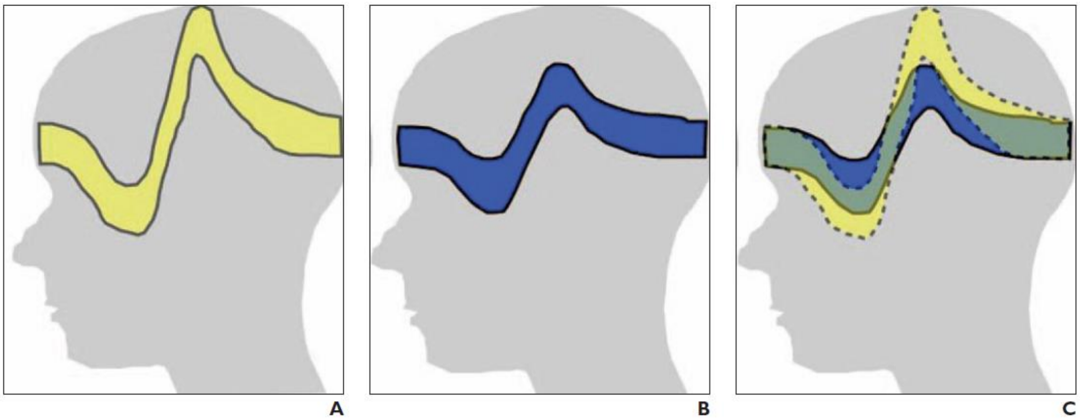

FIG.28: **The effect of bandwidth in slice selection (Adapted from Hargreaves et al, 2011].**

We consider a field homogeneity of Δf(x,z) during slice -selective excitation. Given an RF pulse of bandwidth B_{RF} and slice select gradient of amplitude G_S the excited magnetization m_e is given by the following formula.

$$m_e(x,z) = m(x,z) \cdot \prod\left[\frac{\frac{\gamma}{2\pi}G_S z + \Delta f(x,z) - f_0}{B_{RF}}\right] =$$

$$= m(x,z)\ ) \cdot \prod\left[\frac{z - \Delta z(x,z) - z_0}{S}\right]$$

Z_0 is the nominal slice location excited at transmit frequency $f_0 = \frac{\gamma}{2\pi} G_S z_0$

The through plane shift Δz for field inhomogeneity Δf is

$$\Delta z = -\frac{\Delta f}{\frac{\gamma}{2\pi}G_S} = \frac{\Delta f}{B_{RF}}s$$

$s = 2\pi B_{RF} / (\gamma G_s)$ is the nominal slice thickness. Using thin slices, will reduce the amount of this distortion. The cost of this is both increased scanning time (because more slices are required to adequately cover the volume of interest) and reduced SNR because the voxel size has been reduced. To recover some SNR multiple slices may be averaged during post processing , but this technique reduces the overall efficiency by the square root of the number of the slices averaged.

$\prod(\frac{f}{B_{RF}})$ is the frequency profile of the RF pulse which ideally is rectangular function defined by

$$\prod(\frac{f}{B_{RF}}) = \begin{Bmatrix} 1, & if\ |f| \leq B_{RF}/2 \\ 0, & otherwise \end{Bmatrix}$$

The metal induced inhomogeneities cause the excited magnetization $m_e(x,z)$ to contain spins from different slice location for which $|z-\Delta z(x,z) - z_0| \leq s/2$. The term Δz(x,z) represents the distorted excitation profile caused by field inhomogeneity that corresponds to frequency shift Δf(x,z)

In plane distortion

In most MRI pulse sequences the in-plane spatial information is encoded by two different mechanisms. In the readout direction , spatial information is encoded through frequency. Perpendicular to the readout direction the position of the spins is encoded through phase. Discrete series of gradient pulses is used to produce position depended phase shifts in the phase encoding direction. As we have seen when objects, including the patient or any implant, with non zero susceptibility, is introduced in the magnetic field of an MRI system, an additional magnetic field (usually time independent) is present. The z component of the total field is then given by

$$B_z = B_0 + G_x(t) + G_y(t) + G_z(t) + \Delta B_z(x,y,z)$$

The $\Delta B_z(x,y,z)$ term is the z component of the field of the magnetization induced by the patient and whatever objects are located within and adjacent to the region of imaging. The $\Delta B_z(x,y,z)$ term interferes with the frequency encoding process but does not affect the imaging process at the phase encoding axis. That means that the induced field distorts the image at the readout (frequency encoded) direction and not at the phase encoded direction.

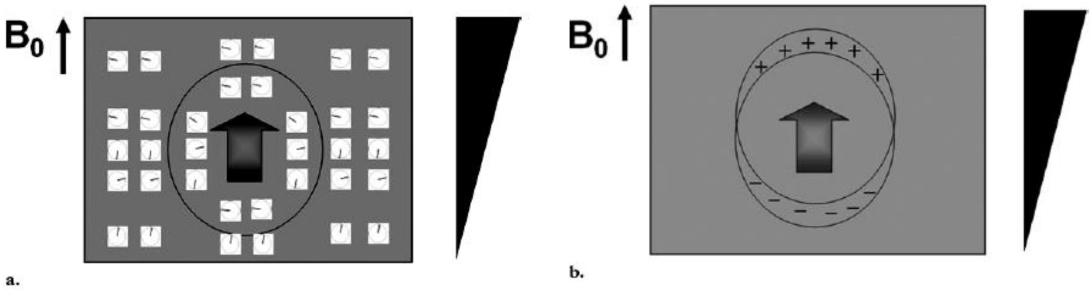

FIG.29:**(a) The spins in the main magnetic field predictably rotate at the same frequency. When the frequency encoding gradient is applied the Larmor frequencies of the spin change along the gradient direction (black triangle) The spins at the location of higher magnetic field (thicker part of the triangle), rotate at higher frequencies. When a metallic object is placed inside the FOV (arrow incide the circle), the spins near the object rotate with higher frequency (b)The region of interest near the metallic object is encoded as if it were at higher gradient location (upper circle) than it actually is. The signal around the region of interest is summed at higher gradient location (+) and subtracted at a lower one. The result is geometric distortion of the object and pill ups and signal loss in the image.[Adapted from Mi-jung Lee et al,2007]**

Position within the object to be imaged are represented by x, y, z.
x' and y' represent positions within the two dimensional image that results. The field frequency f_0 that corresponds to field value B_0 is assigned at image position x'=0. The x' is determined from the measured frequency f by the following formula.

$$f-f_0= \gamma\ [G_R x +\Delta B_z(x,y,z)] \approx \gamma\ G_R x' \text{ or}$$

$$x'(x,y,z) = x + \Delta B_z(x,y,z) / G_R$$

thus the position error is

$$\Delta x = x - x' = \Delta B_z(x,y,z) / G_R$$

It is assumed that the selected slice is perpendicular to the z axis. X is the frequency encoding (readout) direction. Y is phase encoding direction. The frequency f is within the receiver bandwidth. G_R is the strength of the readout gradient.
In the presence of foreign body, $\Delta B_z(x,y,z) \neq 0$, and then $x'(x,y,z) \neq x$. That means that the image is distorted in the direction if the readout gradient
The degree of the distortion is determined by the ratio

$$\boxed{\frac{\Delta B_z}{G_R} \approx \frac{\Delta \chi B_0}{G_R}}$$

We can reduce in plane artifact either by increasing G_R or by decreasing B_0 . However decrease in main magnetic fields strength (B_0), lower signal intensity.
The G_R may be expressed in relation to FOV and receiver bandwidth. The proton resonant frequency is given by Larmor equation.

$$f = \frac{\gamma}{2\pi} B ,$$

where γ is proton's gyromagnetic ratio. The γ/2π is equal to 42.576375MHz/Tesla.
The readout gradient G_R has to produce a frequency variation equal to bandwidth (BW) between the spins of the opposite edges of the field of view(FOV).
The gradient is constant and the magnetic field varies linearly across the x axis. So does the resonant frequency. Therefore

$$f = \frac{\gamma}{2\pi}(B_0+G_R x),$$

where B_0 is the main field strength at the isocenter and x the distance from it.
The difference in resonant frequency equals to bandwidth when we calculate it for the total field of view.

$$BW = \Delta f_{FOV} = \frac{\gamma}{2\pi}(B_0+G_R x_{max}) - \frac{\gamma}{2\pi}(B_0+G_R x_{min})=$$

$$= \frac{\gamma}{2\pi} G_R FOV$$

$$\text{Or } G_R = \frac{2\pi}{\gamma}\frac{BW}{FOV}$$

and if we express γ/2π as f_0/B_0 (the resonant frequency and the magnetic field strength at the isocenter) the above relation is transformed to

$$G_R = \frac{B_0}{f_0}\frac{BW}{FOV}$$

As we have seen earlier when an object is placed in an initially uniform magnetic field, becomes magnetized and produces an induced fields. this fields distorts the initial field. The field induced inside the object is known as demagnetizing field. The induced magnetization and the perturbation in the magnetic field in the general case can be calculated only through numerical methods. However for any ellipsoid object with uniform susceptibility within uniform magnetic field can be calculated through algebraic methods.

The external field of an ellipsoid can not be found in terms of simple functions. The boundary conditions on the surface of the ellipsoid (B_Z continuous to poles, H_Z continuous at the equator can be used to find the maximum (polar) and minimum (equatorial) values of the external field for the general ellipsoid of revolution.
Therefore for the poles

$$\Delta B_z = B_0 \Delta\chi(1-\alpha)/(1+\alpha\Delta\chi) \text{ or } \Delta B_z \approx B_0(1-\alpha)\Delta\chi \text{ for } \Delta\chi \ll 1$$

and for the equator

$$\Delta B_z = - B_0 \alpha\Delta\chi(1+\alpha\Delta\chi) \text{ or } \Delta B_z \approx -B_0\alpha\Delta\chi, \text{ for } \Delta\chi \ll 1$$

α is the demagnetizing factor, a shape dependent number between zero and one. It is related to the magnetic field H_{dm} induced inside an object placed in a magnetic field.
So $H_{dm}= -\alpha M$. A general ellipsoid has three demagnetizing factors one for each principle axis. The sum of the three demagnetizing factors equals to one. For a sphere, due to symmetry reasons it is 1/3 for each axis.

If we assume $|\chi|<<1$ (χ = susceptibility) we may calculate the distortion of the magnetic field inside and outside a sphere, of radius α in the direction of the magnetic field. So it can be proved that

$$\Delta B_Z = 2\Delta\chi/3B_0 \text{, inside the sphere}$$

and

$$\Delta B_Z = \Delta\chi/3B_0{}^3(2z^2-x^2-y^2)/(x^2+y^2+z^2)^{5/2}$$

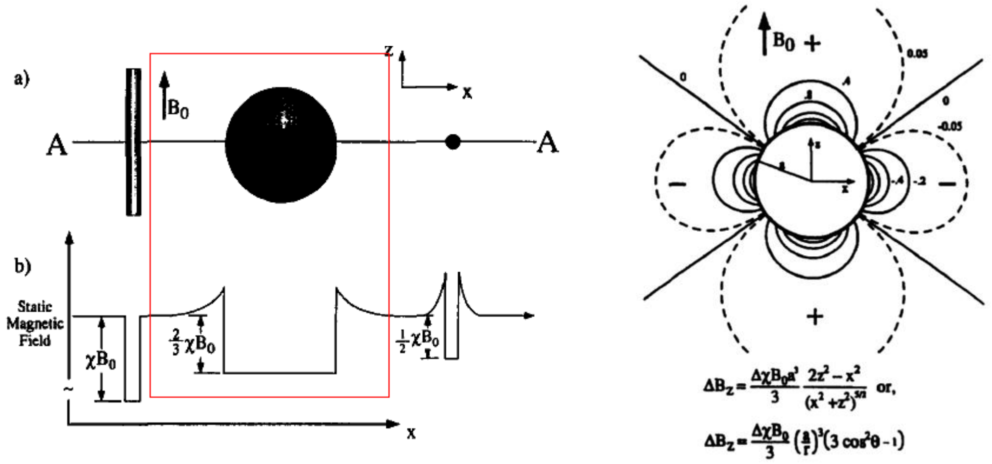

FIG.30: **Field distortion resulting from the presence of a sphere of susceptibility <<1 at magnetic field B_0 [Adapted from John F.Schennck "Role of magnetic susceptibility in MRI",1996]**

As we have seen earlier, at any point in the image, a foreign object produces a position error

$$\Delta x = \Delta B(x,y,z)\ /G_R.$$

For the ellipsoids with $\Delta\chi<<1$, we have calculated the extreme values of $\Delta B(x,y,z)$ at poles are $\Delta B(x,y,z) \approx B_0(1-\alpha)\Delta\chi$ and at the equator $\Delta B(x,y,z) \approx -B_0\alpha\Delta\chi$. So the extreme possible values of $\Delta B(x,y,z)$ are $\pm\ \Delta\chi B_0$.

Therefore the $\frac{\Delta\chi B_0}{G_R}$ is a rough measurement of the maximum position errors Δx_{max} produced when an object of susceptibility $\Delta\chi$ is present. For the ellipsoids the extreme positions errors are

$$\Delta x\ /\ FOV = (1-\alpha)\Delta\chi f_0\ /BW \text{ at the poles and}$$

$$\Delta x\ /\ FOV = -B_0\alpha\Delta\chi f_0\ /BW \text{ at the equator}$$

We may express the variation of B and f across the FOV as fraction of B_0 and f_0, which is about 500ppm. Thus

$$\frac{\Delta x}{FOV} = \frac{\Delta\chi}{500ppm}$$

If we take into account that the FOV is usually divided in to 256 pixels. This corresponds to about 12.5Hz per pixel or 2ppm per pixel if we express it as fraction of f_0. So if $\Delta\chi$ <<1ppm then $\Delta B_{max}/B_0$ and $\Delta f_{max}/\Delta f_0$ are also <<1ppm. The frequency and position errors in this case are less than a pixel and they are negligible. If $\Delta\chi \approx$ 500ppm position errors is also 500ppm which is comparable to FOV and many regions are not represented in the image.

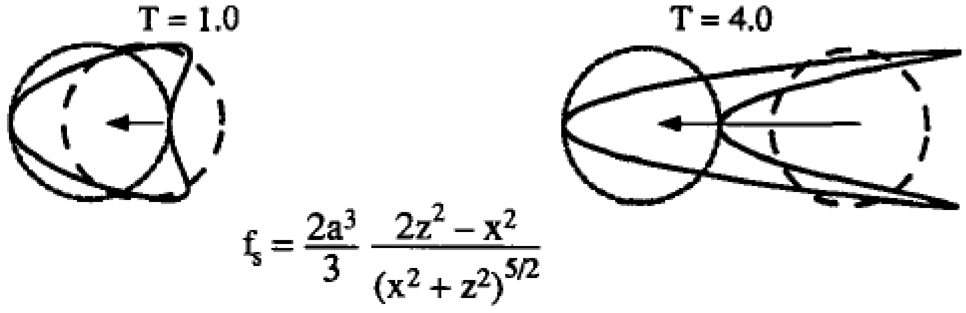

$$f_s = \frac{2a^3}{3}\,\frac{2z^2 - x^2}{(x^2 + z^2)^{5/2}}$$

FIG.31:**Image distortion by sphere at 1.0 and 4.0 in Spin Echo imaging. Adapted from John F.Schennck "Role of magnetic susceptibility in MRI"**

In the figure above, the coarse dashed lines represent the image position for the spins at the surface of a sphere at the absence of field perturbation ($\Delta\chi = 0$). In the presence of field perturbation, spins just inside the sphere surface will be imaged at the circular location defined by the fine dashed line. Spins just outside the sphere surface are mapped to the v-shaped solid lines

T2* effects and failure of fat supression

The magnetic field variations cause resonant frequency variations . When the field changes rapidly with position there is significant dephasing of the signal, resulting in signal loss. We avoid this effect by using pulse sequences from the spin echo family. The 180^0 pulse of spin echo sequences regenerates the lost signal since the 180 pulse refocuses the spins and regenerates the signal, lost by the T2* interactions. However this in not valid for GRE sequences where there is no 180 pulse

Another aspect of the presence of high susceptibility differences, which cause frequency variations is failure of fat suppression techniques that are based on chemical shift or in frequency differences between fat and water tissues.

Optimum susceptibility matching

A foreign object placed in the region of MR imaging should not distort the pre existing magnetic field. That means that the initial magnetization should remain the same. So the susceptibility of the object has to be the same as the susceptibility of the surroundings. If the object is in air the ideal susceptibility is approximately zero ($x_{air} = 0.36x10^{-6}$). When an object is implanted in tissues, which are assumed to have susceptibility equal to that of the water, which is $-9.05x1^{-6}$. Therefore materials with the same susceptibility as tissues, rather than materials with zero susceptibility, are the goal for internal devices.

The ideal implant should have such a combination of paramagnetic and diamagnetic materials that the resultant implant has the optimum susceptibility. However there are not available diamagnetic materials with large negative susceptibilities capable of balancing the large paramagnetic susceptibilities of commonly used materials.

MATERIALS AND METHODS

Materials

All the measurements were made in phantom models. The phantom consisted of a plastic tank filled with tap water. The total water volume was 5lt. In the container was added 5ml of MAGNEVIST (gadopederic acid) of concentration 469mg/ml, obtaining a concetration of 469mg/lt. In this way we tried to simulate the magnetic properties of the soft tissues.
At the bottom of the tank we fixed a frame capable of holding the imaged object. This frame consisted from an acrylic base and two silicon supports where the implant would rest. The supports were placed vertically in the acrylic base and were 32mm high. In the top of the supporter a notch of 2mm depth was created in order to offer better stabilization to the implant. The frame was accurately placed in the middle of the tank

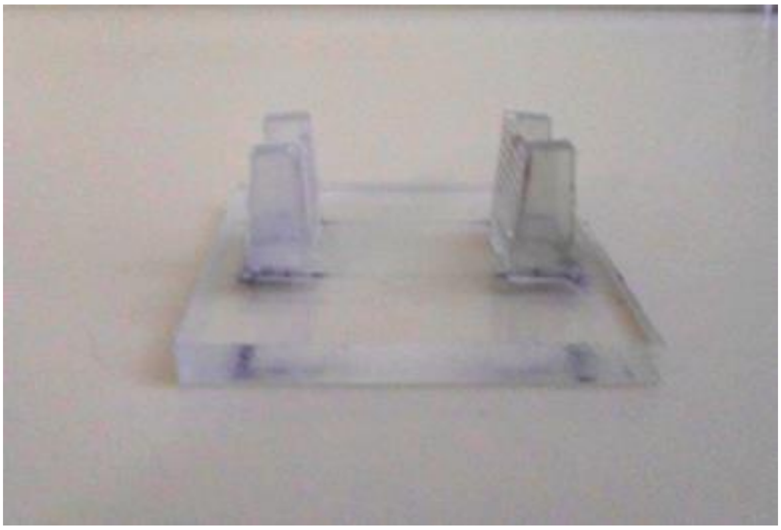

FIG.32: **The acrylic frame used to support the implants.**

We used two metallic prostheses of different composition. The first is a stainless steel Stryker cephalomedullary nail of proximal femur. The second is a titanium locking compression plate by Synthes used in femoral fracture fixation.

FIG.33: **Stryker stainless steel cephalomedullary nail placed inside the tank.**

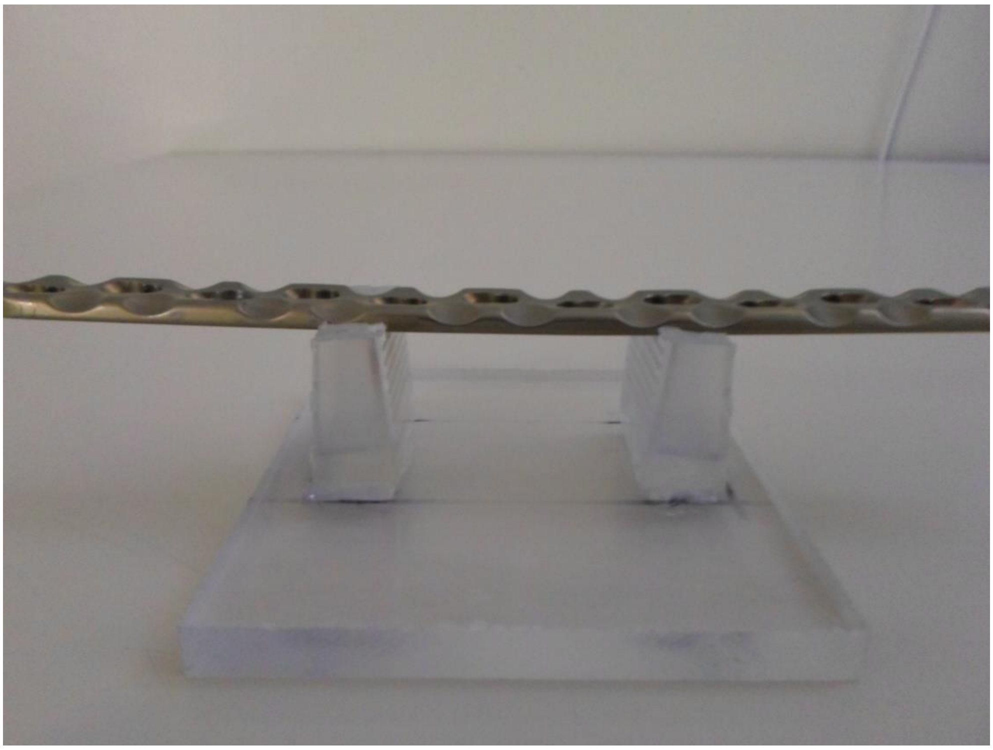

FIG.34: **Synthes titanium femoral LCP.**

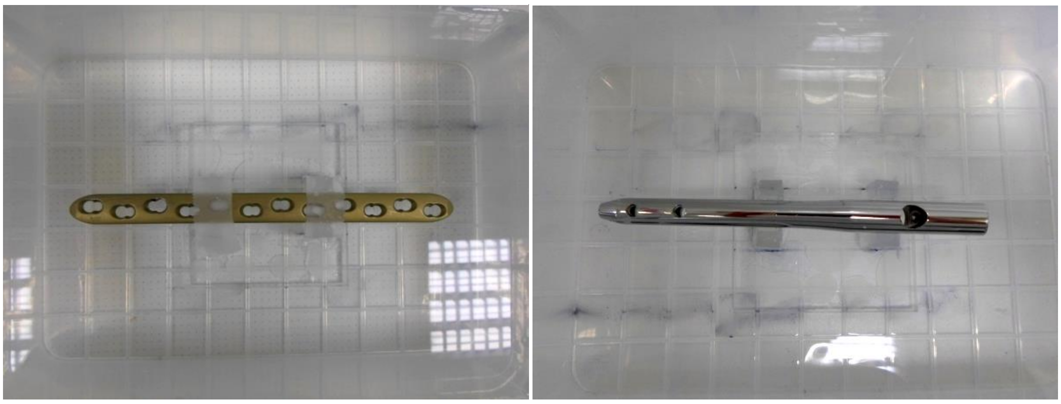

FIG.35:**The same objects as seen from above inside the tank**

MRI images were obtained using a 1.5 T MR scanner (Siemens Magnetom Sonata - Maestro Class, with slew rate 200mT/min and G_R 45mT/m). All the images were acquired using the head coil.The phantom was placed at the isocenter of the MR scanner. The temperature during the measurements was 25^0C. Image processing was carried out in FIJI (win-64). Correlation was analyzed in IBM SPSS statistics 21

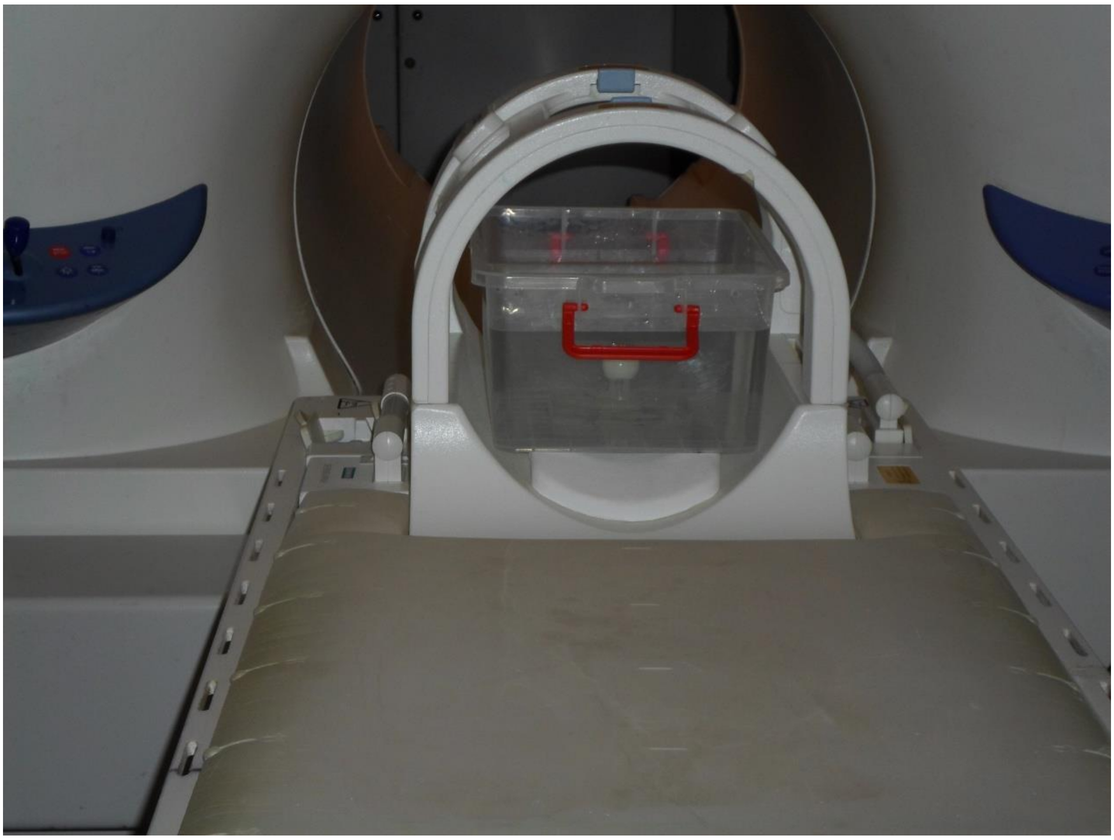

FIG.36: **The phantom placed inside the head coil**

Methods

The segmentation of images derived from in vivo mri acquisitions is very demanding. The number of the anatomical structures depicted and the variety of signal intensities in such images increase the complexity and the difficulty of the task. Phantom derived images are more suitable for segmentation. These images can be segmented in three regions. The regions of signal pill ups, with high intensity signal, the region of signal void with hypo intense regions and artifact free regions. The presence of the metallic materials, as we have seen, creates distortion in the magnetic field. This distortion is responsible for the artifact generation. In fact we expect more intense artifact, where the distortion is higher. So we may suppose that the gradient magnitude of the grayscale image represents the region of greater distortion and artifact. The gradient magnitude is high when the change in the gray scale image is high regardless if the region has high or low intensity signal.

Gradient magnitude is the first derivative of the image, and is performed along some preferred direction, assuming also a spatial neighborhood support. The result returned by the *Gradient Magnitude* operation gives the largest gradient magnitude when every possible direction is taken into account. It is a non negative number computed as

$$\sqrt{(\frac{\partial f(x,y)}{\partial x})^2 + (\frac{\partial f(x,y)}{\partial y})^2}$$

When the gradient magnitude operator has been applied, the higher values at the resulting image will correspond to the more abrupt alterations of the signal regardless if it comes from signal voids or signal pill ups. So if we set a threshold in the resulting image we can describe regions of the artifact both of high and low intensity. This is very convenient since we transform the complicated task of segmentation, to an image gradient thresholding problem.

The selection of a threshold affects the accuracy and the efficiency of the image segmentation. The basic assumption behind setting a threshold in an image is that the object and the background can be distinguished by comparing their gray value levels with suitably selected threshold value [C. H. Li and C. K. Lee 1993]. We can classify thresholding algorithhms as local and global. The local algorithms select threshold based on the local properties of the histogram.

This type of algorithms are affected more from noise and often need some kind of preprocessing in order to enhance the local maxima and minima. The global methods algorithms measure global criteria of the histogram as criteria for the selection. These methods are less prone to noise.

We thought that global techniques are more suitable for our task since they are less prone to noise. From the global techniques the most known are Otsu's method, minimum cross error approach and minimum cross entropy. Otsu's method is considered gold standard for image thresholding. It is based in the on the within class variance, between class variance and total variance of gray levels. The main drawback of this method is the bias in the

threshold when the two populations have unequal variances or when the populations of the two distributions are very different.
The minimum error approach was rejected because it assumes normal distribution of the two populations. We had no reason to assume that in our case.

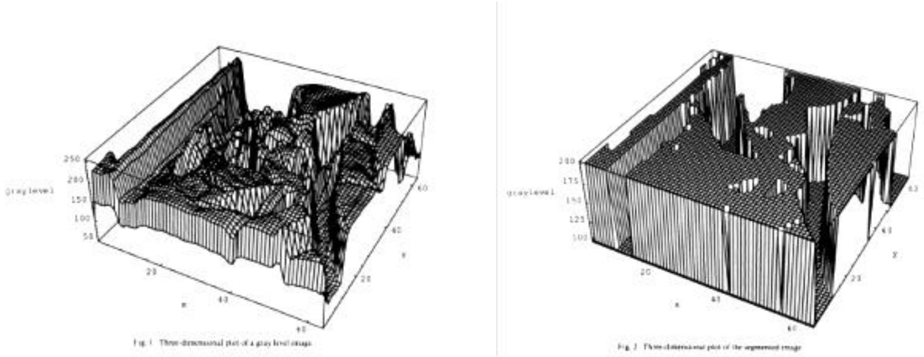

Fig. 1 Three-dimensional plot of a gray level image

Fig. 2 Three-dimensional plot of the segmented image

FIG.37 :**Three-dimensional plots of the gray level and segmented image through the minimum cross entropy method used [C. H.Li and C. K.Lee 1993].**

Minimum cross entropy is evolved from maximum entropy method. In maximum entropy method we select the solution that allows the maximum entropy within the limit of the constraints (the constraints limit the solution set to those who are consistent with the data). It is considered unbiased and allows maximum freedom. Cross entropy measures the theoretic distance between two distributions P = {p_1, p_2...p_N} and Q = {q_1, q_2..q_N} by

$$D(Q,P) = \sum_{k=1}^{N} q_k \log_2 \frac{q_k}{p_k}$$

The formula above can be explained as the expectation of the change in the information content when we use P instead of Q. Minimum cross entropy can be seen as an extension of maximum entropy method by setting equal initial estimates for all p_i when no prior information is available. (C. H. Li and C. K. Lee 1993). Minimum cross entropy was selected as an unbiased, non parametric method which gives good results in thresolding without the need of apriori knowledge

The use of the gradient magnitude on the image, is mainly an edge detecting method. By using this operator we do not intend to fully segment any area of the image containing artifact, but mainly to use it as a reliable estimator of the artifact extent. In other words we propose a fully automatic algorithm of image thresholding, which can be used to compare the artifact under different conditions in phantom models. The use of mathematic algorithms in every step without any observer involvement, makes it reproducible and more objective. Another advantage, except that it is fully automated, is that there is no need to any reference to the real dimensions or composition of the implant. Thus we talk for a relative quantification of the artifact and as such a method should be tested.

In the following Figure the 3D reconstruction of the artifact generated from a stainless steel Gamma Nail is shown (through gradient magnitude and Minimum cross entropy thresholding) in green color.

FIG.38 :**Three-dimensional plots of the gray level and segmented image through the minimum cross entropy method used**

It is well known from the theory above, that the artifact size is reduced, as the pixel bandwidth increases. Misregistration error Δx, in x axis is proportional to the difference in susceptibility between the implant and the phantom substrate Δχ and irreversibly proportional to the frequency encoding gradient

$$\Delta x \sim \frac{B_0 \Delta\chi}{G_R}$$

Let us suppose that we take two acquisitions of the same material, under the same pulse sequence differing only in the bandwidth. We know that the image received in the lower bandwidth to have much more artifact compared to that in the higher bandwidth. The cost we pay by reducing the artifact through bandwidth increase, is the decrease of signal to noise ratio (SNR) as a result of noise augmentation. However, we make the assumption that the noise discrepancy is negligible compared to the signal intensity of artifact difference.

Our basic hypothesis is the result of the subtraction between the two images acquired in two different bandwidths should have-correlate with the resulting area difference between the thresholded images derived with the method described above. Failure of correlation would suggest that our algorithm is not suitable for relative quantification of the susceptibility induced artifact in phantom models

The subtraction of two identical images will result in an image matrix full of zeros. (We do not take in account any noise differences). The mean signal from the image matrix that results from this subtraction is zero. As the differences between two images increase, the mean signal of the image, also increases. The mean signal of the resulting image integrates both variations both in area of and signal intensities of the artifact.

$$Q(i,j) = P_1(i,j) - P_2(i,j)$$

where $P_1(i,j)$ is low bandwidth acquisition and $P_2(i,j)$ is high bandwidth acquisition.

The mean signal value μ of the resulting image Q(i,j), of MxN pixels is defined from its normalized histogram

$$\mu = \sum_{k=0}^{L-1} r_k p(r_k)$$

were r_k is gray level value and p(r_k) its probability density function from its normalized histogram. Since we will not deal with noise we do not have to estimate the energy of the image as in ***[Kolind et al, 2004]***.

Almost the same procedure is followed for the segmented images. Since the signal intensities have been taken in account in the thresholding procedure, we care only for the area above the threshold. So we convert our images to binary mask and then we subtract the image acquired at high bandwidth from that at low bandwidth. We expect good correlation between the mean signal from the images resulting from the subtraction of the original images, with the area discrepancy between the segmented images

We tested two metal implants, a stainless steel gamma nail and a titanium LCP plate. We acquired images at GRE and SE pulse sequences. Then we worked one representative slice of each sequence, usually the medium slice. Next, we correlated the results of the image subtractions described above. The sequences selected are all used in the musculoskeletal MR imaging. The most of them are axial (transverse (TRA)) and the rest coronal (COR)

SE -TSE: 2D or 3D turbo spin echo. From literature, TSE is the sequence that gives the best results relative to artifact reduction except in the case that dedicated metal artifact reduction sequences are available (such as SEMAC and MAVRIC). (*Jin-Suck Suh et* al, *Tao et al, Port et al, Koff et al)*. In SE family a 90^0 pulse flips the net magnetization vector in transverse plane. As the nuclei go through T1 T2 and T2* relaxation the transverse magnetization is gradually dephased. An 180^0 pulse is applied at time one half of TE to rephase the nuclei and form an echo. This 180^0 pulse refocusing tends to reverse the t2* inhomogeneity effects. In conventional SE techniques one line of k-space is filled at time. In TSE the initial 90^0 pulse is followed by a series of 180^0 pulses which makes possible the simultaneous filling of multiple lines of k-space. TSE techniques thus, are faster. SE and TSE techniques are the main used in musculoskeletal MRI

VIBE: It is a volume interpolated GRE. The outer k space contains information about the details within the image - high spatial frequencies. Omitting data collection from this areas results in truncation artifacts. In VIBE these lines of k -space are filled with zeros. By this doing so artifact reduction is obtained as well as partial volume effects are improved. However spatial resolution is not improved

PSIF: PSIF belongs to the balanced steady state free precession se quences, which are part of the family of GRE techniques. The dephasing induced by each applied gradient is compensated for by a gradient of opposite polarity resulting in unique T2/T1 contrast. It has high SNR and excellent tissue contrast but it is very sensitive to susceptibility effects. It requires very good B_0 homogeneity. PSIF is a backward running FISP, which generates only the spin echo component of the balanced gradient echo

PSIF has found clinical application at musculoskeletal system for acquisition of diffusion weighted images of the spine. For example PSIF may be used to differentiate a metastasis from an acute benign compression fracture, since metastases show high diffusion rate. Metastasis generally demonstrate high signal intensity on diffusion weighted images. However sclerotic metastases (such as prom prostate cancer) do not show hyperintensity in PSIF scans

CISS: Constructive Interference in a Steady State. A true FISP (Coherent GRE) with dual excitation. When certain echo paths of a balanced SSFP are out of phase during data acquisition, signal voids occur, especially in areas with differences in magnetic susceptibility. CISS was developed for area s of high variable susceptibility. The CISS technique is composed of 2 3D balanced SSFP acquisistions measured in succesion. By slightly vaying excitaion pulses, the destructive interference patterns (signal voids) are spatially shifted from each other in the images. A complex algorithm is used to add the two images. Signal voids are filled with data from the second image and SNR is improved at a factor of $\sqrt{2}$. Heavily T2w 3D CISS is often has high spatial resolution and submillimeter partitions offer detailed delineation of small structures. Improvements in magnet homogeneity have allowed this imaging techniques to be expanded in areas such as the spine. Excellent cerebrospinal to soft tissue contrast provides improved depiction of the dorsal and ventral cervical nerves as they traverse the thecal sac

HASTE: Half acquisition Single Shot Turbo Spin Echo. Combines half Fourier technique with fast spin echo imaging. With Haste each slice is acquired and even reconstructed before the next slice acquisition has begun. This is accomplished by acquiring an echo train length equal to the required phase encoding steps for one slice. It is very rapid (<2sec per slice) and it is used to reduce motion artifact and in patients with poor cooperation.

In the following Tables 2 & 3 we see the main parameters of the acquisitions used. At the first one of the following tables (2), the acquisition parameters regarding the stainless steel gamma nail, (pulse sequence, weight, pixel bandwidth, plane, TR , TE and slice thickness) are shown

Table 2: STAINLESS STEEL GAMMA NAIL ACQUISITION PARAMETERS

Pulse Sequence	*Weight*	*Pixel BW (Hz)*	*Plane*	*TR (msec)*	*TE (msec)*	*Slice thickness (mm)*
T2_TSE_TRA_b50	T2	50	TRA	4140	116	2
T2_TSE_TRA_b100	T2	100	TRA	3400	102	2
T2_TSE_TRA_355	T2	355	TRA	3400	102	2
T2_TSE_TRA_b780	T2	780	TRA	3400	102	2
PD_TSE_TRA_b100	PD	100	TRA	3400	15	2
PD_tse_TRA_b780	PD	780	TRA	3400	15	2
PD_vibe_fa05n_TRA_b130	PD	130	TRA	9,49	4,63	2
PD_vibe_FA05_TRA_b850	PD	850	TRA	9,49	1,58	2
T1_vibe_FA15n_TRA	T1	130	TRA	9,49	4,63	2
T1_vibe_FA15N_TRa	T1	850	TRA	9,49	1,58	2
T2_3Dpsif_TRA	T2	100	TRA	13,6	6,57	0,6
T2_3Dpsif_TRA	T2	1150	TRA	13,6	2,48	0,6

COR: Coronal TRA: Transverse TR: Repetition time TE: Echo time BW: Bandwidth

The same parameters are displaced in table (3), for the titanium plate.

Table 3: TITANIUM PLATE ACQUISITION PARAMETERS

Pulse Sequence	*Weight*	*Pixel BW (Hz)*	*Plane*	*TR (msec)*	*TE (msec)*	*Slice thickness (mm)*
T2_tse_TRA_b50	T2	50	TRA	4140	116	2
T2_tse_TRA_b100	T2	100	TRA	3400	102	2
T2_tse_TRA_b355	T2	355	TRA	3400	102	2
T2_tse_TRA_b781	T2	780	TRA	3400	102	2
T2_tse_COR_b100	T2	100	COR	3400	102	2
T2_tse_COR_b781	T2	780	COR	3400	102	2
T1_tse_TRA_b100	T1	100	TRA	500	15	2
T1_tse_TRA_b781	T1	780	TRA	500	15	2
PD_tse_TRA_b100	PD	100	TRA	3400	15	2
PD_tse_TRA_b781	PD	780	TRA	3400	15	2
PD_vibe_fa05n_TRA	PD	130	TRA	9,49	4,63	2
PD_vibe_fa05n_TRA	PD	850	TRA	9,49	1,58	2
PD_vibe_FA15n_TRA	PD	130	TRA	9,49	4,63	2
PD_vibe_FA15n_TRA	PD	850	TRA	9,49	1,58	2
se_tra_b40	T1	40	TRA	500	31	2
se_tra_b781	T1	780	TRA	500	31	2
t2_3Dciss_COR_b130	T2	130	COR	9,26	4,18	0,6
t2_3Dciss_COR_b1149	T2	1150	COR	4,3	1,87	0,6
t2_3Dpsif_COR_b100	T2	100	COR	13,6	6,57	0,6
t2_3Dpsif_COR_b1149	T2	1150	COR	13,6	248	0,6
haste_diff_slcdg_tra	diffusion	100	COR	1820	106	2
haste_diff_slcdg_tra	diffusion	780	COR	1820	104	2
3DT2_tse_TRA_b100	T2	100	TRA	3000	113	2
3DT2_tse_TRA_b781	T2	780	TRA	3000	113	2

In the following Figures we are going to see step by step the procedure followed for the stainless steel gamma nail and for the titanium plate for the TSE pulse sequences and for BW=50Hz/pixel and BW =780Hz/pixel.

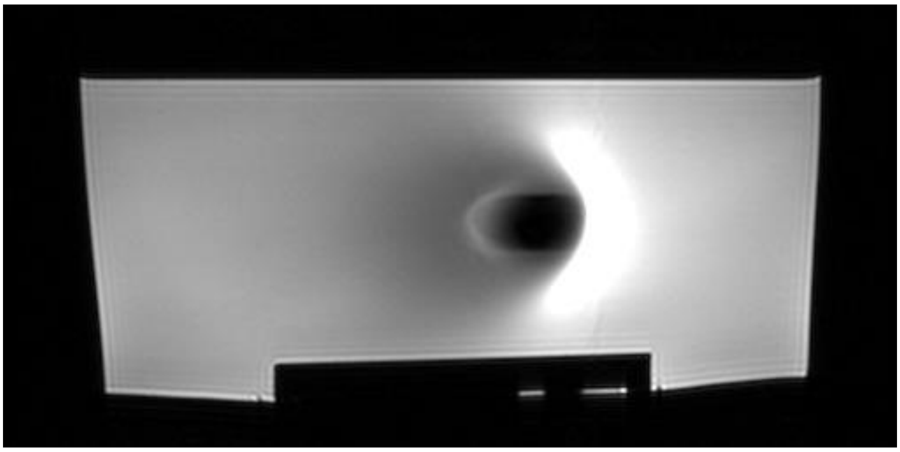

FIG.39: **Representative axial slice of the stainless steel implant at BW =50Hz/pixel (TSE)**

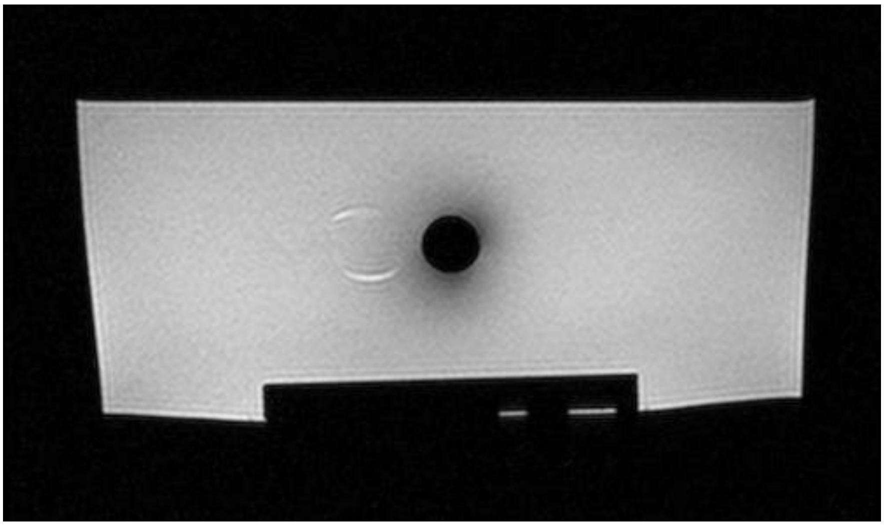

FIG.40:**The same axial slice of the stainless steel implant at BW=780Hz/pixel (TSE)**

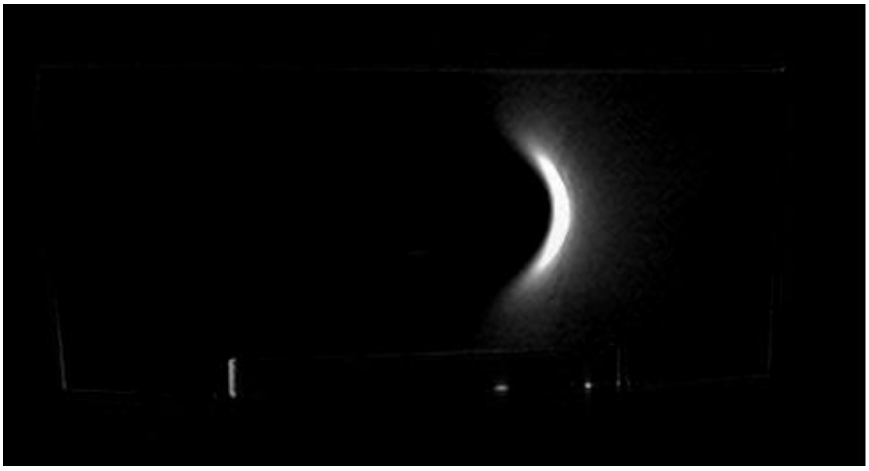

FIG.41:. **Subtracting FIG.40 from FIG39. In this image we calculate mean gray value. The remaining signal is considered to be the difference between the artifact in the two images**

FIG. 42: **Gradient magnitude of FIG.39 - axial slice of the stainless steel implant BW =50Hz/pixel (TSE)**

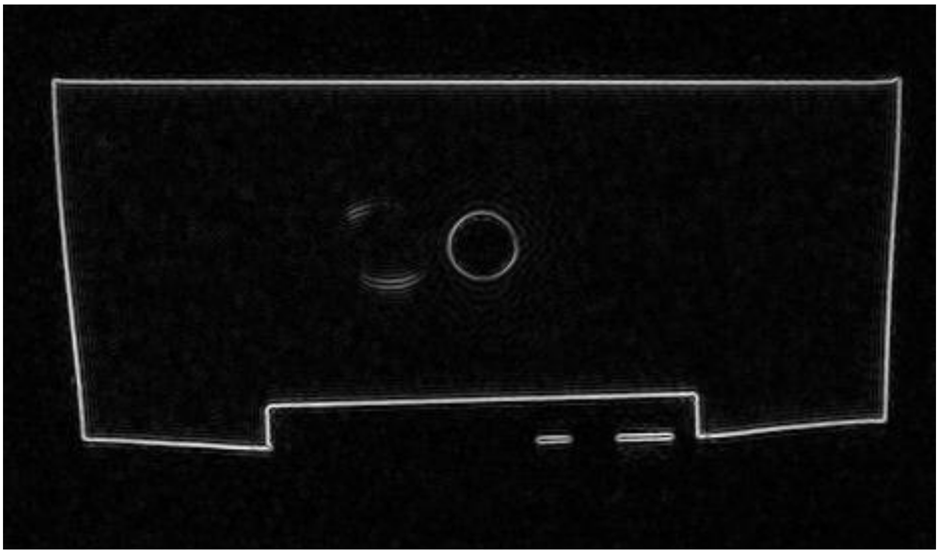

FIG. 43: **Gradient magnitude of FIG.40 - axial slice of the stainless steel implant at BW=780Hz/pixel (TSE)**

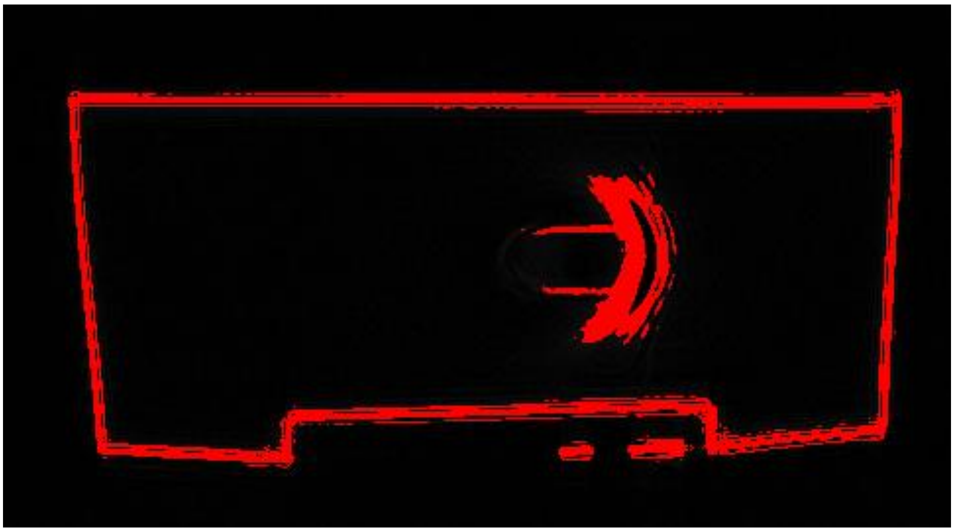

FIG. 44: **Minimum cross entropy application in FIG.42 axial slice of the stainless steel implant BW =50Hz/pixel (TSE)**

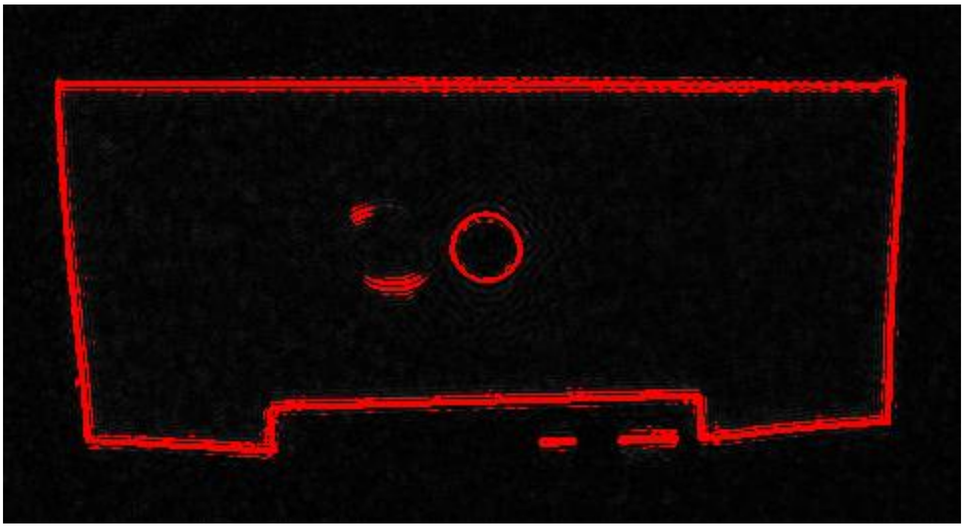

FIG. 45: **Minimum cross entropy application in FIG.43 - axial slice of the stainless steel implant at BW=780Hz/pixel (TSE)**

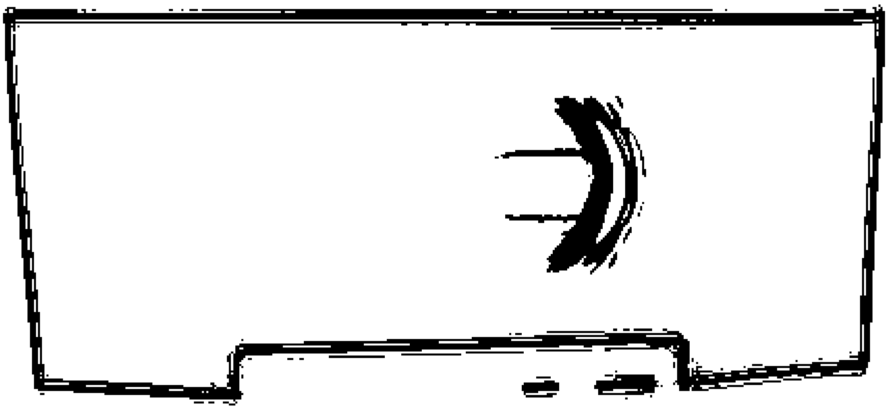

FIG. 46: **FIG.44 converted to mask (binary image) BW =50Hz/pixel (TSE)**

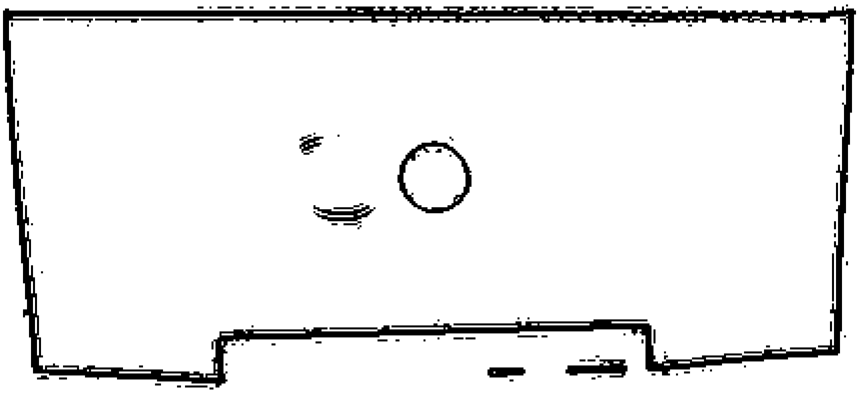

FIG. 47: **FIG.45 converted to mask (binary image) BW=780Hz/pixel (TSE)**

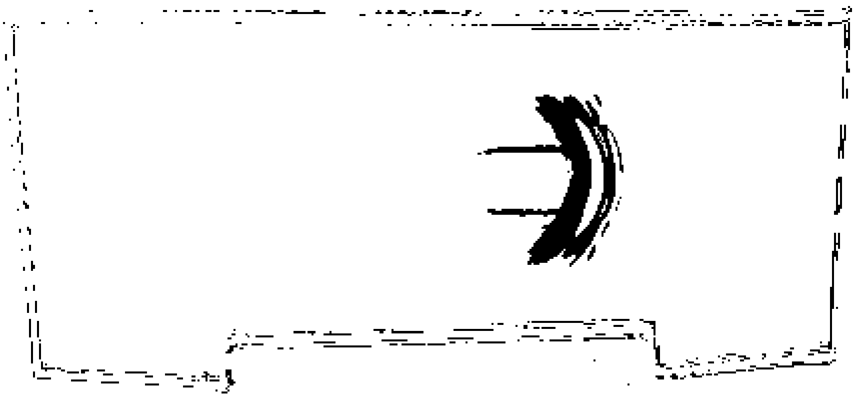

FIG. 48: **Subtraction of FIG.45 from FIG.44 (high BW acquisition from low). The resulting area has to correlate with the mean gray value from the subtraction of the original images (FIG.41)**

Following, we will show briefly the same procedure for the LC titanium plate, this time for coronal slices.

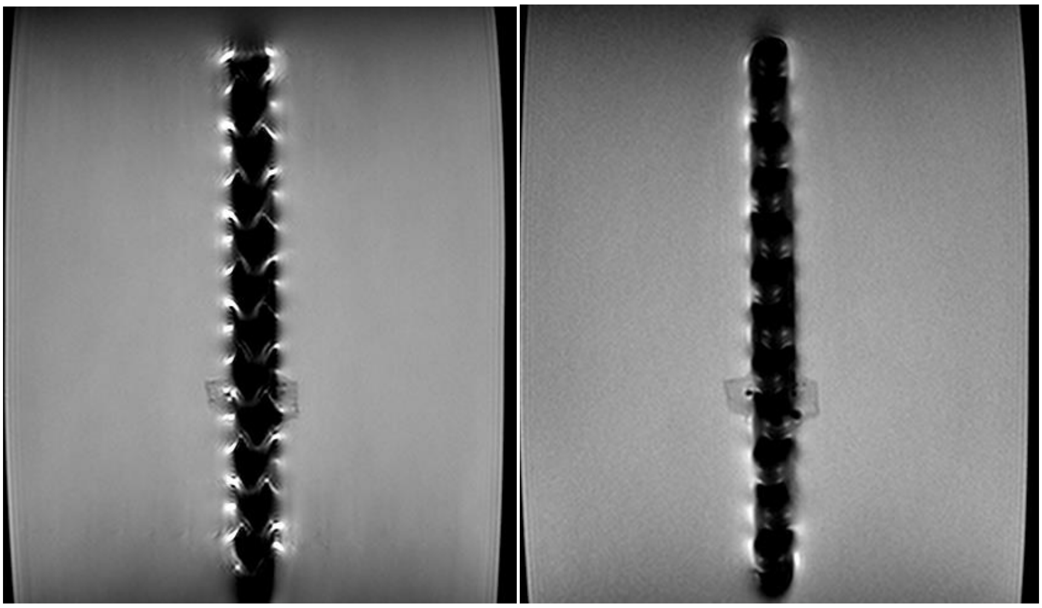

FIG.49: **original acquisitions of titanium LCP plate at 100 and 780 Hz/pixel**

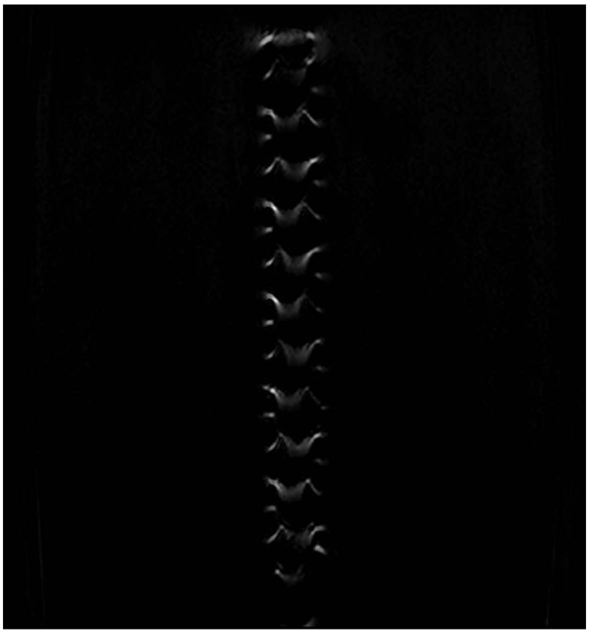

FIG.50: **The image that results when we subtract the high BW image from the low BW image. In this image we measure the mean gray value**

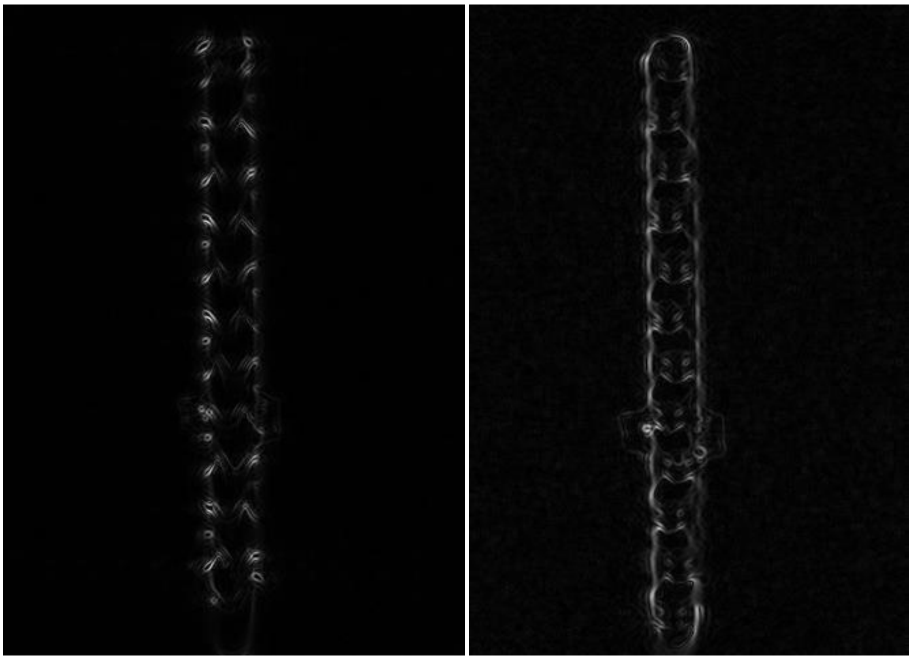

FIG. 51: **Applying gradient magnitude (low BW /high BW) - titanium LCP plate**

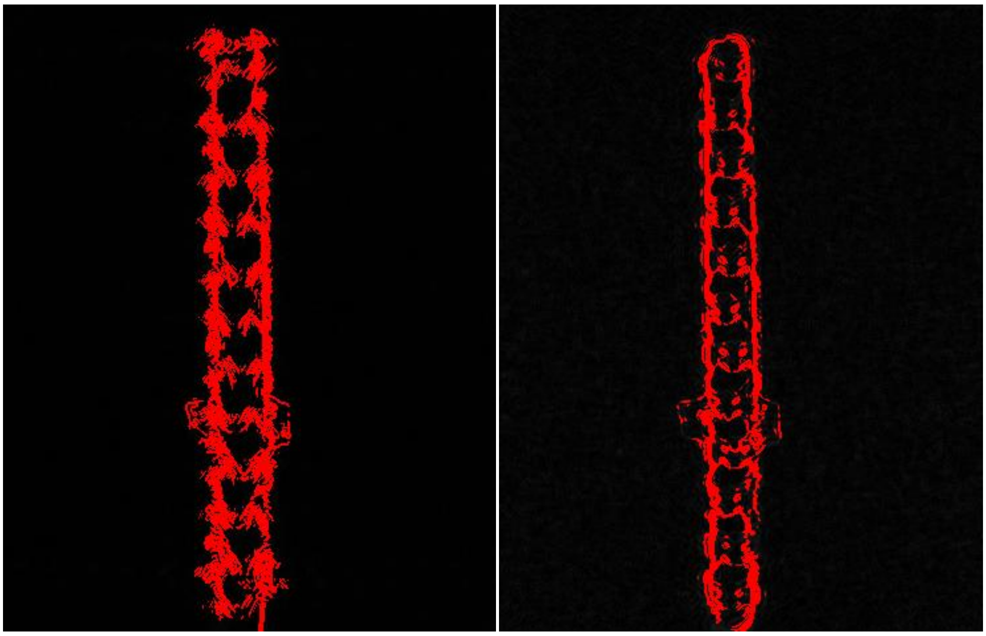

FIG.52: **Applying minimum cross entropy threshold (low BW /high BW), at FIG.51**

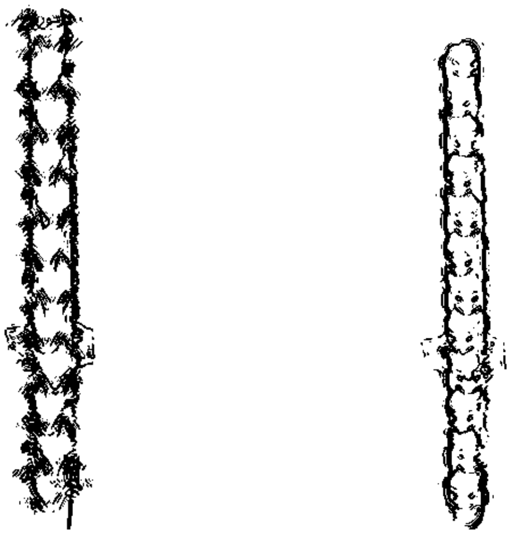

FIG.53: **Conversion to mask (low BW /high BW)**

FIG.54: **The binary image resulting from the subtraction of the thresholded images of FIG.53 (lowBW -high BW)**

RESULTS

In the following Tables 4 & 5 we present the results of the measurements, considering always the middle- slice (coronal or axial) of a stack for each pulse sequence tested.

Table 4: TITANIUM PLATE ARTIFACT QUANTIFICATION BY THE PROPOSED AND THE REFERENCE METHOD: single slice

PULSE SEQUENSE	Mean grayscale value from image subtraction	Area from thresholded image subtraction (%)
T2_tse_TRA_b50 -780	7,59	0,917
T2_tse_TRA_b100 -780	2,447	1,301
T2_tse_TRA_b355 -780	7,5	0,247
T2_tse_COR_b100-780	29,412	2,838
T1_tse_TRA_b100-780	2,114	0,864
PD_tse_TRA_b100-780	6,064	0,772
PD_vibe_fa05n_TRA _b130-850	2,841	0,509
PD_vibe_FA15n_TRA_b130-850	5,816	0,518
se_tra_b40-780	9,615	1,104
t2_3Dciss_COR_b130-1150	101,626	11,214
t2_3Dpsif_COR_b100-1150	151,549	3,257
haste_diff_slcdg_tra_b100-780	12,786	4,821
3DT2_tse_TRA_b100 -780	3,049	0,75

TABLE 5: STAINLESS STEEL GAMMA NAIL ARTIFACT QUANTIFICATION BY THE PROPOSED AND REFERENCE METHOD: single slice

PULSE SEQUENSE	Mean grayscale value from image subtraction	Area from thresholded image subtraction(%)
T2_tse_TRA_b50 -780	27,523	1,572
T2_tse_TRA_b100 -780	20,84	1,012
T2_tse_TRA_b355 -780	9,074	0,525
PD_tse_TRA_b100-780	11,681	1,104
PD_vibe_fa05n_TRA _b130-850	5,094	2,473
PD_vibe_FA15n_TRA_b130-850	6,303	2,299
t2_3Dpsif_TRA_b100-1150	78,056	2,839

The values calculated above, as we have seen, originate from representative slices (one from each pulse sequence). Then we correlated the mean signal intensity differences, resulting from image subtractions from the highest bandwidth acquisition of a sequence, with the percentage areas resulting from the subtractions of the corresponding gradient thresholding method proposed . The results are shown in Tables 6-13 below, considering both parametric (Pearson correlation) and non-parametric (Spearman's rho) tests for pooled data of the experiments, i.e. stainless steel and titanium. At tables 6,7 the results presented, have been derived correlating the data from the stainless steel gamma nail and the plate together

Table 6: Correlations (parametric) - STAINLESS STEEL GAMMA NAIL & TITANIUM LCP PLATE: single slice

		VAR00001	VAR00002
VAR00001	Pearson Correlation	1	,607**
	Sig. (2-tailed)		,005
	N	20	20
VAR00002	Pearson Correlation	,607**	1
	Sig. (2-tailed)	,005	
	N	20	20

**. Correlation is significant at the 0.01 level (2-tailed).

Table 7:Correlations (non parametric) - STAINLESS STEEL GAMMA NAIL & TITANIUM LCP PLATE: single slice

			VAR00001	VAR00002
Spearman's rho	VAR00001	Correlation Coefficient	1,000	,634**
		Sig. (2-tailed)	.	,003
		N	20	20
	VAR00002	Correlation Coefficient	,634**	1,000
		Sig. (2-tailed)	,003	.
		N	20	20

**. Correlation is significant at the 0.01 level (2-tailed).

Both parametric and non parametric tests above, show medium positive correlation between the two methods (the proposed and the reference one

The same procedure has been repeated for all slices of one pulse sequence at two bandwidths (50 and 780Hz/pixel). We preferred an axial T2w -TSE, since it is the most common in use for musculoskeletal imaging. The transverse plane gives as much more slices than the coronal, due to longitudinal shape of the implant. The implant is a Howmedica - Stryker stainless steel Gamma nail

In the following Table 8 the mean signal intensity of all images of a stack resulting from the subtraction of corresponding slices at the two bandwidths selected is shown, as well as the corresponding percentage area differences resulting from the subtraction of the thresholded gradient images.

Table 8: STAINLESS STEEL GAMMA NAIL ARTIFACT QUANTIFICATION BY THE PROPOSED AND THE REFERENCE METHOD: All slices for the axial TSE sequence

Slice number	Mean grayscale value from image subtraction	Area from thresholded image subtraction(%)
1	39.645	2.906
2	41.426	3.094
3	42.051	3.247
4	40.537	3.214
5	38.137	2.984
6	35.822	2.724
7	34.227	2.386
8	32.586	2.182
9	30.210	2.016
10	27.141	1.728
11	24.245	1.545
12	22.263	1.373
13	19.183	1.215
14	14.673	1.055
15	11.418	1.073
16	10.560	1.171
17	10.338	1.255
18	10.487	1.364
19	10.808	1.456
20	11.167	1.485
21	11.309	1.475
22	11.058	1.578
23	10.666	1.746

In the following Table 9, we can see the results of the correlation between them:

Table 9: Correlations (parametric)- STAINLESS STEEL GAMMA NAIL: all slices

		VAR00001	VAR00002
VAR00001	Pearson Correlation	1	,914**
	Sig. (2-tailed)		,000
	N	23	23
VAR00002	Pearson Correlation	,914**	1
	Sig. (2-tailed)	,000	
	N	23	23

**. Correlation is significant at the 0.01 level (2-tailed).

Table 10: Correlations (non parametric) - STAINLESS STEEL GAMMA NAIL: all slices

			VAR00001	VAR00002
Spearman's rho	VAR00001	Correlation Coefficient	1,000	,802**
		Sig. (2-tailed)	.	,000
		N	23	23
	VAR00002	Correlation Coefficient	,802**	1,000
		Sig. (2-tailed)	,000	.
		N	23	23

**. Correlation is significant at the 0.01 level (2-tailed).

In this case, parametric and non parametric tests show strong positive correlation

We will repeat the same procedure for axial slices of the Synthese titanium plate. Again we will take the differences between two BW (100Hz /pixel and 780Hz/pixel). The pulse sequence tested is again TSE since this sequence is the best common sequence available for imaging when implants are present.

Table 11: TITANIUM PLATE ARTIFACT QUANTIFICATION BY THE PROPOSED AND THE REFERENCE METHOD: All slices for the axial TSE sequence

Slice number	Mean grayscale value from image subtraction	Area from thresholded image subtraction(%)
1	7.834	1.258
2	7.953	1.252
3	7.668	1.223
4	7.496	1.164
5	7.242	1.135
6	7.874	1.196
7	8.032	1.267
8	7.547	1.194
9	6.726	1.036
10	7.015	1.064
11	7.590	1.113
12	7.682	1.163
13	7.671	1.125
14	7.295	1.034
15	7.132	1.012
16	7.588	1.042
17	7.394	1.030
18	7.361	1.105
19	8.050	1.165
20	8.228	1.115
21	8.230	1.115

Table 12: Correlations (parametric) - TITANIUM LCP PLATE: all slices

		VAR00001	VAR00002
VAR00001	Pearson Correlation	1	,608**
	Sig. (2-tailed)		,003
	N	21	21
VAR00002	Pearson Correlation	,608**	1
	Sig. (2-tailed)	,003	
	N	21	21

**. Correlation is significant at the 0.01 level (2-tailed).

Table 13: Correlations (non parametric) - TITANIUM LCP PLATE: all slices

			VAR00001	VAR00002
Spearman's rho	VAR00001	Correlation Coefficient	1,000	,623**
		Sig. (2-tailed)	.	,003
		N	21	21
	VAR00002	Correlation Coefficient	,623**	1,000
		Sig. (2-tailed)	,003	.
		N	21	21

**. Correlation is significant at the 0.01 level (2-tailed).

Moderate positive correlation is shown between the two methods for the titanium LCP plate

DISCUSSION

In this thesis we tried to propose a new method capable of detecting susceptibility artifacts in phantom models. The problem was converted from the demanding segmentation task, to the more feasible of thresholding using the physics of susceptibility artifact. This was possible by creating a new image derived from the gradient magnitude of the initial, assuming that the distortions in the magnetic field creating the artifact, would result in corresponding changes in the image gray level. This step was crucial in order to segment two very different areas of the artifact, those of high intensity signal and those of low intensity signal. Next the image was thresholded and converted to binary. By this way we manage not only to quantify the artifact, but also to give its spatial location in the image. The method was fully algorithmic and automatic in all the steps. This is the main advantage of the method since it is observer independent and fully repeatable. These characteristics make the method suitable for standardization procedures and quality controls.

The proposed algorithm had to be tested with another method considered a reference. Most of the methods described in the previous pages were either based on observer's vision or used selected threshold values without sufficient justification.
We consider the idea of image subtraction of ***[Kolind et a 2004],*** as the most objective one. We did not deal with the noise, assuming it to be negligible, so we worked using the gray values of the image instead of its energy.

Every measuring process needs a reference standard. Kolind et al, ***[Kolind et a 2004],*** used a wax replica for the implants, obtaining in this way a reference image with no susceptibility artifact. However our reference point has not always to be zero. Since it is well known from theory that the high BW acquisitions have lower susceptibility artifact, we used the highest bandwidth acquisition as reference.

The correlation between the two methods of artifact quantification–provided medium to strong correlations. The correlation was tested both with the use of parametric and non parametric test, giving similar results. The most suitable approach is the use of non parametric tests, since we have no data of the statistical properties of the artifact areas. The first group which was correlated contained a representative slice from all the pulse sequences tested, specifically the middle ones . Medium positive correlation was demonstrated. One reason for not obtaining strong correlation might be the heterogeneity inside this group. The group was composed GRE and SE pulse sequences and included both stainless steel and titanium implants

The next correlation tests performed regarded images from the same implant and the same pulse sequences but considering all slices of a stack. Specifically, we tested all axial slices of a TSE sequence of the stainless steel G-nail and titanium LC plate. For the first strong correlation were derived, while for the second one the correlation obtained was medium. So other reasons than the variability that concerns the implants or the pulse sequences may be responsible. We have to take in to consideration some limitations of our study.

First of all the gradient magnitude detects the abrupt changes in the image intensity, which correspond to changes in the magnetic field in the image. Nevertheless the artifact may have areas with little or no change at all, especially if we talk for signal voids. The gradient magnitude describes best the limits of the artifact than the artifact per se. The algorithm has to be completed with an additional algorithm, capable of distinguishing areas of common image features, inside the limits set by the gradient magnitude and segment them as artifact areas. This could be a future task. Such a method could be applicable not only to phantom models but also to clinical practice. At the other hand the initial image subtraction gives a quantification of the area of the artifact and not its margins.

Another limitation is that the reference image is not free of artifact. The artifact does not follow some kind of symmetry or regularity. In other words, although the image with the lower BW has higher overall artifact, when we subtract the images the areas of the artifact may or may not coincide.

Another problem concerning the gradient magnitude of the image is that it does not discriminates the origin of the gradient at the image. Any area of abrupt change in image intensity may be thresholded as artifact. Such an area is the air -phantom interface. If however we view it from its physical perspective, we have to admit that it is a region of susceptibility difference and therefore its segmentation as an artifact area is correct.

Finally, every segmentation algorithm may be prone to error at low SNR images This is true and for this method. The selection of a global thresholding technique, makes it less prone to erroneous segmentation within reasonable limits.

The method proposed here accounts for a promising technique, since it is automated and thus less subjective than other methods proposed. It can be used mostly as estimator of the artifact rather than an absolute quantification process. For this reason it is proposed for relative quantification of images of the some pulse sequence. The combination with segmentation methods, exploiting image features in regions of signal voids or pile ups, has the potential to provide a very powerful tool of artifact quantification with the additional advantage of precise spatial localization and delimitation.

REFERENCES

1. Augustin et al. "MRI of large non ferromagnetic metal implants at 1.5 T", Journal of Comp Ass Tom 11(4):678-683.

2. Bitar et al. "MR pulse sequenses" Radiographics (2006) 26:513-537.

3. Hargreaves et al. "Metal induced artifacts in MRI" AJR Sept (2011).

4. Haruki Imai et al. "Three- dimensional quantification of susceptibility artifacts from various metals in magnetic resonance images", Acta Biomaterialia (2013) 8433-8439.

5. Hayter et al. "MRI after arthroplasty:Comparison of MAVRIC and conventional FSE techniques, AJR:197 (2011).

6. Jin-Suck Suh et al"Minimizing artifacts caused by metalic implants at MRI", AJR:171, (1998).

7.Koch et al. "A multispectral 3D aquisistion technique for imaging near metal implants" Magnetic Resonance in Medicine vol 61(2) 381-390 (2009).

8. Koff et al. "Quantifying image distortion of orthopedic materials in mri", JMRI (2013) Sep;38(3):610-8.

9. Kolind Sh et al. "Quantitative evaluation of metal artifact reduction techniques", Journal of magnetic resonance imaging 20:487-495 (2004).

10. Kurtz et al. "Prevelance of total hip and knee arthroplasties in the united states from 1990 through 2002", J Bone and Joint Surg Am (2005); 85: 1487-1497.

11.C. H Li and C. K. Lee "Minimum entropy thresholding", Pattern recognition vol 26 No 4pp 617 625 1993.

12. Matsuura et al. "Quantitive analysis of magnetic resonance imaging susceptibility artifacts caused by neurosurgical biomaterials: Comparison of 0,5 1,5 3,0 Tesla magnetic fields", Neurol. Med. Chir. (Tokyo) 45 395-399 (2005).

13. Mi-jung Lee et al. "Overcoming artifacts from metallic orthopaedic implants at high field strength MR imaging and multi detector CT ", Radiographics (2007) 27:791-803.

14. Oldendorf William, "MRI primer" Raven Press (1991).

15. Port et al "Quantification and minimization of magnetic susceptibility artifacts on GRE images", Journal of Comp. Ass. Tom. 24(6):958-964 (2000) .

16. Randall Olsen et al. "Metal artifact reduction sequence", Radiographics (2000), vol 20 699-712.

17. Resnick D. "Diagnosis of bone and joint disorders", Saunders (2002).

18. Rudish et al. "Metallic artifacts in MRI of patients with spinal fusion: A comparison of implant materials and imaging sequenses" ,Spine vol23(6) (1998).

19. Runge et al. "The physics of clinical MR taught through images" Thieme, (2013).

20. Sang-Youn g Zho et al. "Artifact reduction from metallic dental materials in T1w spin echo imaging at 3 tesla" JMRI (2012).

21.Schennck J. Review article "Role of magnetic susceptibility in MRI", Medical Physics Vol.23 N_o 6 (1996).

22. Spaldin N. "Magnetic materials Fundamentals and device applications", Cambridge University Press (2003)

23. Sutherland-Smith et al, "Magnetic resonance imaging metallic artifact of commonly encountered surgical implants and foreign materials", Vet. Radiol. Ultrasound Vol 53 No3 (2012) 312-317.

24. Takeuchi et al. "The orientation of orthopaedic metallic devices relative to the frequency encoding gradient affects susceptibility artifacts: An experiment using open mr imaging" Fukuosha Acta Med. 102 (5) 185-191 (2011).

25. Tao Ai et al. "SEMAC -VAT and MSVAT-SPACE sequence strategies for metal artifact reduction in 1.5T MRI" Investigative radiology vol47 (2012).

26. Vandevenne et al. "Reduction of metal artifacts in musculoskeletal mr imaging", *Journal* Belge de Radiologie (2007),90:345-349.

27. Wenmiao Lu et al. " SEMAC: Slice encoding fro metal artifact correction in MRI", MR in medicine 62:66-76 (2009).

28. Westbrook et al. "MRI in practice", 4th edition Wiley-Blackwell (2011) .

29. White LM et al. "Complications of total hiparthroplasty: MR imaging initial experience", Radiology 2000 215 254-62.

30. Z. H. Cho. "Total inhomogeneity correction including chemical shifts and susceptibility by view angle tilting", Med. Physics 15; 1 (1988).

31. Κωσταρίδου Ε Παναγιωτακης Γ. "Ιατρική απεικονιση με ακτίνες Χ: Προβολική απεικόνιση, υπολογιστική τομογραφία και ποιοτητα ιατρικής εικόνας", Εργαστήριο Ιατρικής Φυσικής Πανεπιστήμιο Πατρών (Σημειώσεις, Μάρτιος 2011)

32. Μάζης Αλκίνοος. ΦΥΣΙΚΗ ΤΟΜΟΣ 3 Εστία (1963) .

33. Μαρής Θ. "Γενική εισαγωγή στην απεικόνιση μαγνητικού συντονισμού" Εργαστήριο Ιατρικής Φυσικής Πανεπιστήμιο Κρήτης (Σημειώσεις, 2011)

34. Ioannis Vrachnis, George Vlachopoulos, Anna Karahaliou, Thomas Marris and Lena Costaridou. A method for quantifying metal artifacts in MRI, 8th European Conference on Medical Physics (ECPM 2014), 11-13 September 2014, Athens, Greece.

Internet sources

1.web_ http://homepages.engineering.auckland.ac.nz/~kacprzak/notes.htm
2.web_bigwww.epfl.ch/thevenaz/differentials "image differentials"
3. web_homepages.inf.ed.ac.uk/rbf/HIPR2/pixsub.htm
4. web_http://mri-q.com/4-or-more-rf-pulses.html
5. web_http://www.ndt.net/article/ndtce03/papers/v062/v062.htm "Practical Applications of NMR in Civil Engineering"
6. web_http://www.reddit.com/r/Elements/comments/g9op9/magnetism_and_magnets_part_2_filling_orbitals
7. web_http://www.revisemri.com/questions/equip_qa/measuring_snr "Measuring SNR"
8.web_www.usa.siemens.com/healthcare "MRI acronyms"